Alma Mater Studiorum · Università di Bologna

Scuola di Scienze

Dipartimento di Fisica e Astronomia

Corso di Laurea Magistrale in Fisica

4D-treatment with patches and rescanning in Proton Therapy

Relatore:

Prof.ssa Maria Pia Morigi

Correlatore:

Dott. Jan Hrbacek

Presentata da:

Lorenzo Lasagni

Anno Accademico 2017/2018

Nobody ever figures out what life is all about, and it doesn't matter. Explore the world. Nearly everything is really interesting if you go into it deeply enough.

Richard P. Feynman

Abstract

The aim of this study, carried out at the Center for Proton Therapy of the Paul Scherrer Institute (Villigen, Switzerland), involves the verification of the possibility of 4D treatments on patients requesting a patch field. This technique is used when the dimensions of the area to be irradiated are greater than 12 cm for the T direction and 20 cm for the U direction. We also went to research the setup that provides a better dose homogeneity, in order to mitigate the tumor's motion during the treatment.

Three clinical cases were studied with the motions obtained from the respective 4DCT. Moreover, one of these was analyzed again simulating a motion extrapolated from a 4D-MRI. All 4 cases were analyzed in 9 combinations, 3 possible rescan scenarios (1, 4 and 8 rescan) and 3 different overlapping setups between the two patches (0, 1 and 2 cm of overlap). The values obtained were compared to the 3D plan. The dose homogeneity measures (D5-D95 and V95) showed that in the case of a slight motion (under 2 mm) there was no need to intervene with motion mitigation. For the motions classified of medium intensity (2-10 mm), it was found the need to introduce motion mitigation. In none of the previous cases, a systematic benefit emerged with a certain pattern of patch overlap. It was not possible to fully evaluate the last case, having a large motion (about 20 mm), as it needed an IMPT plan (technique not yet developed for the 4D), but still indications, regarding the benefit of the use of 8 rescan and greater possible overlap, emerged. The experimental measurements obtained at Gantry 2 with the use of a 2D detector (Octavius 1500 XDR), a gating system and a Quasar motion platform, confirmed that there are no problems with the actual dose release. The homogeneity of the dose is also found when there are extreme conditions, such as 2 cm overlap, 8 rescan and 4 patches (for a 4 cm zone receiving 32 rescan) and a strong simulated motion.

Sommario

Lo scopo di questo studio, svolto presso il Center for Proton Therapy del Paul Scherrer Institute (Villigen, Svizzera), prevede la verifica della possibilità di effettuare trattamenti 4D su pazienti richiedenti un patch field. Tale tecnica viene utilizzata quando le dimensioni della zona da irraggiare sono maggiori di 12 cm per la direzione T e di 20 cm per la direzione U. Si è, inoltre, andati a ricercare il setup che fornisse una miglior omogeneità di dose. Sono stati studiati tre casi clinici con i moti ottenuti dalle rispettive 4DCT. Inoltre, uno di questi è stato analizzato nuovamente simulando un moto estrapolato da una 4D-MRI. Tutti e 4 i casi sono stati analizzati in 9 combinazioni, 3 possibili scenari di rescan (1, 4 e 8 rescan) e 3 diversi setup di sovrapposizione dei due patch (0, 1 e 2 cm di sovrapposizione). I valori ottenuti sono stati messi a confronto con il piano 3D. Le misure di omogeneità della dose (D5-D95 e V95) hanno mostrato come nel caso avente un moto di lieve entità (circa 2 mm) non vi fosse necessità di intervenire con mitigazione del moto. Per i moti classificati di media intensità (2-10 mm), si è riscontrata la necessità di introdurre una mitigazione del moto. In nessuno dei casi precedenti è emerso un beneficio sistematico con una determinata configurazione della sovrapposizione del patch. Non è stato possibile valutare a pieno l'ultimo caso, avente un moto di grande entità (circa 20 mm), in quanto necessitava di un piano IMPT (tecnica ancora non sviluppata per il 4D), ma ha comunque dato indicazioni riguardanti il beneficio dell'utilizzo di 8 rescan e una maggiore sovrapposizione possibile. Le misurazioni sperimentali ottenute presso Gantry 2 con l'utilizzo di un rivelatore 2D (Octavius 1500 XDR), un sistema di gating e una piattaforma mobile Quasar, hanno confermato che non vi sono problemi per quanto riguarda l'effettivo rilascio della dose. L'omogeneità della dose si è riscontrata anche quando ci sono delle condizioni estreme, come 2 cm overlap, 8 rescan e 4 patch (per una zona di 4 cm ricevente 32 rescan) e un forte moto simulato.

Contents

Part I

Background

Introduction

Hadron therapy is the radiotherapy for cancer treatments that uses heavy charged particle, hadrons, if only protons are used it is called proton therapy. Thanks to the control for size, shape, and depth, due to no exit dose, proton therapy is emerging as therapy of choice over conventional radiotherapy. Research is starting to study treatment involving organs like lungs and liver. These organs at risk presents complications, such as the presence of many critical structures that lie close to the target, and the presence of motion. Many techniques have been developed to mitigate the intrafraction motion, but the level of 3D treatments has not been reached yet. In the course of this thesis, that has been carried out for a duration of 6 months in the Center for Proton Therapy at Paul Scherrer Institute (Villigen, Switzerland), we have studied the feasibility to deliver 4D treatments that required patches.

In the delivery of proton therapy, it is sometimes necessary to split a field into two or more parts, since the dimensions of the target volume exceed the deliverable size of the gantry. In 4D cases this can be particularly problematic since the patching zone moves during the irradiation; the introduction of motion mitigation is therefore necessary. In order to verify the feasibility of 4D treatments with patches, we developed a new tool to permit the dose visualization of a single patch, a new version of the TPS for the 4DDC, a new procedure to deliver experimental verifications and a new version of the MATLAB script to evaluate the mid-ventilation phase in case of metastasis.

In chapter 1 of the thesis it is exposed a short introduction to proton therapy, with

particular attention to the physics behind it and the biological effects induced by the proton beam. A quick view on history and a brief introduction to cyclotron are also explained.

In chapter 2 the attention is initially on the PSI facilities, after that it goes more into the specifics of our problematics like the planning of the dose and the theory behind 4D treatments. The last part of the chapter will be fundamental to understand why and how the experimental work was done.

In chapter 3 it is explained what patch fields are and how the 4D dose calculation works, as those were the specific parts of the 4D workflow that were changed in the course of the thesis work. After a brief introduction to the clinical cases used, results are exposed with a discussion about how they were generated and what indications emerge from them.

In chapter 4 the experimental verifications are explained, showing the experimental setup used and the results. A discussion of the results follows at the end of the chapter. Possible outlooks for future investigations are proposed in the last paragraph called conclusions.

Chapter 1

Proton therapy

1.1 History

The history of external radiotherapy begins in 1895, thanks to Emil Grubbe, who used X-rays to treat a woman with a carcinome of the breast, just one year after their discovery. Since radiation therapy was becoming more and more important in oncology, many improvements were done in the following decades. Since the beginning of the twentieth century, the main issue was the reduction of the dose to healthy tissues while maintaining the prescribed dose to the target. Fractionated radiation therapy was an initial step, and after that in the thirties it began the study about the dose deposition of different types of particles. In 1946 for the first time the use of protons was suggested by R. R. Wilson [1], but it was only in the next decade that first treatment on patient started and just in nuclear physics research facilities. A disadvantage of this technique was in the low energy achievable by the accelerators; in fact, as they were not designed specifically for treatments, they didn't permit to treat deeply seated tumors. At the beginning of the sixties, the facilities started to treat a bigger set of tumor classes, especially the brain tumor, but it was just in 1970, with the introduction on the clinic use of Computed Tomography (CT), that the dose calculation started to be more accurate

and the proton therapy started to be used in a hospital. The world's first hospital-based proton therapy center was the Massachusetts General Hospital (MGH), opened in the late Seventies, that made the first treatment in 1970, followed by Paul Scherrer Institute (PSI) in 1984. Subsequently, a low energy cyclotron center for ocular tumors at the Clatterbridge Center for Oncology in the UK, opened in 1989, followed by Loma Linda University Medical Center in California in 1990. In Italy there are currently 3 centers: CATANA (in Catania, hadron-therapy only for ocular tumors), CNAO (Centro Nazionale di Adroterapia Oncologica, in Pavia) and the IBA center in Trento. Another center is actually under construction in Rome and should start the firsts treatments in 2020. The traditional indications for proton therapy have been treatments of head and neck, brain, and prostate cancer, but growing results from its application for other cancer types are proving to be positive. In 2013, 105743 patients [2] were treated with proton therapy, a number that is anticipated to grow larger and faster as new proton therapy centers continue to open within the next several years.

1.2 Physics of Proton therapy

A proton is a subatomic particle, with a positive electric charge and it is a basic component of the nucleus of atoms. Protons have three main types of interactions with matter: scattering, stopping and nuclear interactions [3]

Scattering Scattering is explained by a theory that concerns the deflection caused by electromagnetic interaction between atomic nuclei and protons. The effect of a single nucleus interaction is countless, but as the number of nuclei is extremely high, it is possible to see an effect and therefore the outcome will have a statistical nature. Since the scattering is due to the electromagnetic force it is also known with the name "multiple Coulomb scattering". The effect is a lateral spread out of the proton beam, and the statistical outcome, due to the central limit theorem, is similar to a Gaussian. It is not

possible to assume the outcome as a normal Gaussian, because large single scatters in the target are not rare enough. Typical values of the related half-width are around a few degrees, with 16 in the worst scenario [3].

Stopping Stopping is explained by a theory that concerns the interaction between atomic electrons and protons and it induces a slowdown of the beam. This is the key feature of the advantage of using protons: they do not have an exit dose because beyond the stopping point the dose can be considered negligible.

A new quantity, called range, defined as the mean path length of protons with initial energy E_0 in the matter, is formulated in the continuous slowing down approximation

$$R = -\int_{E_0}^{0} \frac{dE}{dE/dx} \tag{1.1}$$

.

Stochastic nature of the energy loss causes the range straggling, in a mono-energetic proton-beam, all protons will stop more or less at the same depth, with a slight spread in the stopping point. The effect will be more visible if the original beam has a spread in energy. The straggling is around 1.2% of range and it slightly changes between light and heavy materials [4].

Concerning the theory of stopping a characteristic rate of energy lost by protons emerges, described by the so-called stopping power. Due to the fact that protons stay longer in the vicinity of electrons when they are slower, they will also interact more and lose more energy [3].

Nuclear interactions Nuclear interactions are not only of one type, and they are not explained by a single theory. It is also really difficult to model them in a proper way, but luckily their biological effect is really small and, with some approximation we still have a good comprehension of the environment, such that we can design radiotherapy treatments safely. Nonelastic interactions result to be the most interesting ones, because

they produce secondary particles: charged (protons and α) and not charged (neutrons and γ-rays). The effect of those particles will be a larger spread of the dose deposition, due to their bigger emission angles.

1.3 Bethe-Bloch formula

The quantity called stopping power, or simply dE/dx, was initially calcutaled by Bohr, with a classic approach, giving this relation:

$$-\frac{dE}{dx} = \frac{4\pi z^2 e^4}{m_e v^2} N_e \ln \frac{\gamma^2 m_e v^3}{z e^2 \bar{v}} \tag{1.2}$$

while the quantum mechanic results were formulated by Bethe and Bloch. The Bethe-Bloch formula, here presented in the full version with density correction δ and shell correction C, is:

$$\frac{dE}{dx} = 2\pi N_a r_e^2 m_e c^2 \rho \frac{Z}{A} \frac{z^2}{\beta^2} \Big[\ln \Big(\frac{2 m_e \gamma^2 v^2 W_{max}}{I^2} \Big) - 2\beta^2 - \delta - 2\frac{C}{Z} \Big] \tag{1.3}$$

where r_e is the classic electron radius, m_e is the electron mass, N_a is the Avogadro number, I is the average potential of eccitation, Z is the atomic number of the material hit, A is the number of mass of the material hit, is the density of the material, z is the charge of the incident particle in e unit, $\beta = v/c$ of the incident particle, $\gamma = 1/\sqrt{1-\beta^2}$, W_{max} is the maximum energy that can be transferred in a single collision.

The two corrections are important respectively at high and low energies. The δ correction comes from the polarization of the atoms along the path of the carged particles, induced by their electric field. This effect becomes important when the energy of the particle increase and it also depends on the density of the material hit.

Shell correction C takes into account an effect that comes into play when the speed of the particles is close, or even smaller, than the atomic electrons one. In this case, it is no more possible to assume the electron with no motion respect to the beam, so that we have to add this correction.

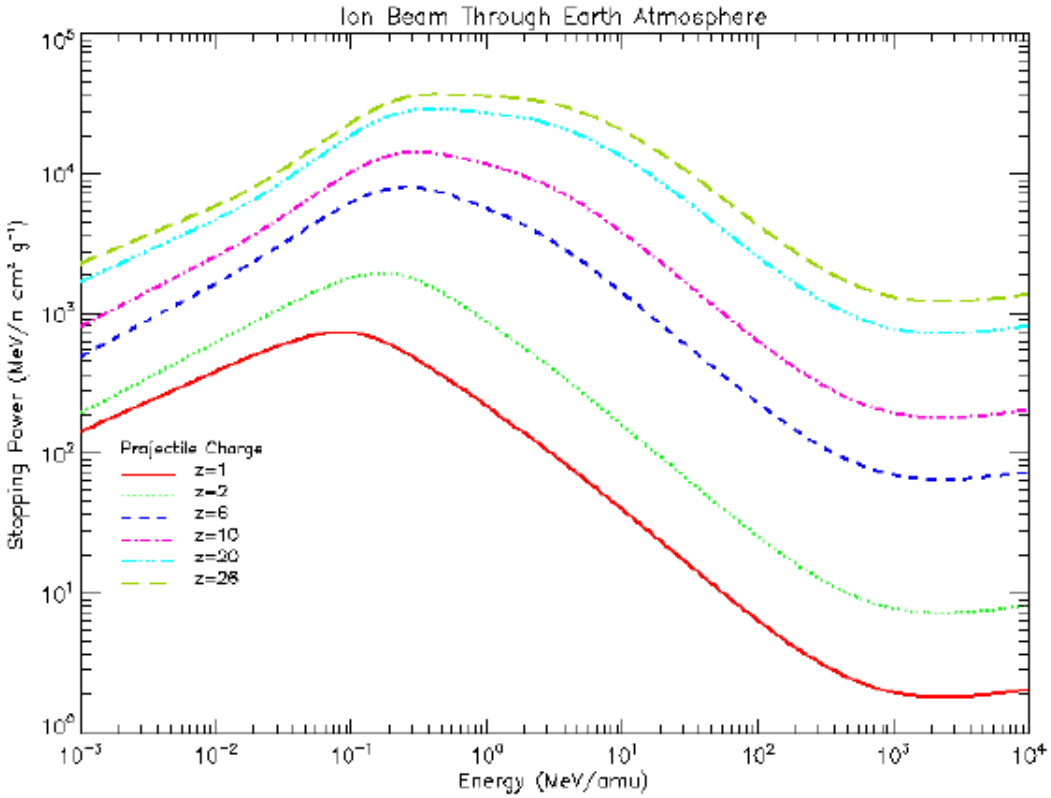

Figure 1.1: Stopping power of different ions in function of different energies. [?]

In Figure 1.1 the stopping power of different ions is presented in function of the energy. It is easy to see that, for non-relativistic energies, dE/dx is principally dominated by the $1/\beta^2$ factor that decreases when the energy increases. This trend has an important variation when $v \simeq 0.96c$, the stopping power reaches a minimum. After this spot the $1/\beta$ factor keep constant and the dE/dx increase again following the log of the formula 1.3.

Analyzing Figure 1.1 it is clear that a heavy charged particle will have a bigger stopping power when its kinetic energy is smaller and that it will slow down while it penetrates more trough the matter. The main consequence is that the particle releases more energy per unit of length at the end of the path than at the beginning, as can be seen in Figure 1.2 that shows a Bragg curve for an alpha particle in air.

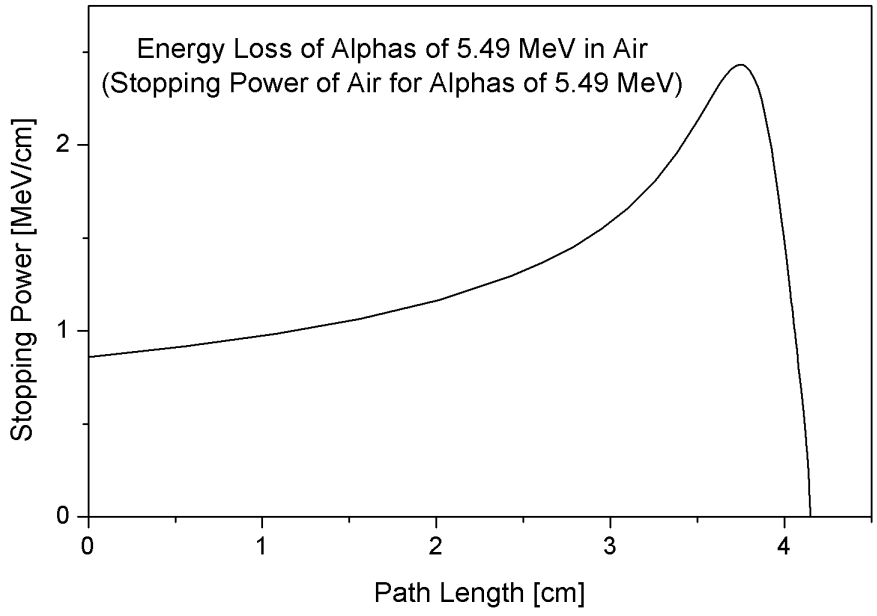

Figure 1.2: Typical Bragg curve that shows the variation of the stopping power in function of the path in matter.

Thanks to this way of interacting we can assume that charged particles, or in this case specifically protons, give the great advantage to be easily controllable in all three dimensions, while with photons it was possible just with two of them and moreover it is not easy.

Currently, for analytical dose planning algorithm in particle therapy, a new quantity, Relative Proton Stopping Power (RPSP), is considered, that is the stopping power ratio $\hat{S}$ of a medium relative to water. It can be approximated without shell and density correction by the following formula [5]:

$$\hat{S} \equiv \frac{S}{S_w} \approx \frac{\rho_e}{\rho_{e,w}} \cdot \frac{\ln\left(\frac{2m_e c^2\beta^2}{I(1-\beta^2)} - \beta^2\right)}{\ln\left(\frac{2m_e c^2\beta^2}{I_w(1-\beta^2)} - \beta^2\right)} = \hat{\rho_e} \cdot f(\beta, I, I_w)\,. \tag{1.4}$$

The RPSP, for energies above 15 MeV/nucleon, can be considered largely energy independent, as its dependence is below 0.4% [6], while below this limit it is ignored by most analytical dose planning systems. For this reason, considering a mean particle energy equal to 200 MeV/nucleon and setting the mean excitation value of water at 75 eV, equation 1.4 can be approximated to:

$$\hat{S} \approx \hat{\rho_e} \cdot \frac{12.77 - \ln I}{8.45}\,. \tag{1.5}$$

1.4 Biological effects of ionizing radiation

Radiation is classified into ionizing and not ionizing based on its ability to ionize the medium. Ionizing radiation can be divided into two main categories:

- Directly ionizing: radiation produces ions directly (protons, $\beta^{\pm}$);
- Indirectly ionizing: radiation produces ions in an indirect way (X-rays, γ, neutrons).

1.4.1 DNA damage

Biological damage caused by radiations results from the ionization of atoms forming molecular structures of cells in living organisms. An ionized atom will tend to produce new chemical bonds within the molecule to which it belongs. The vital functions of the cell can be compromised if the damaged molecule is critical within the cell.

Deoxyribonucleic acid, DNA, is a nucleic acid that contains the genetic information necessary to the biosynthesis of RNA and protein molecules essential, for the development and proper functioning of most living organisms. DNA is formed by four different nitrogenous bases: two purine bases (Adenine and Guanine) and two pyrimidine base (Thymine and Cytosine) which, assembled in groups of three (triplets), are organized into chains of nucleotides forming the various genes located on chromosomes. Each gene provides for the coding of a particular protein. Each triplet determines a well-defined amino acid into the protein. Any errors occurring in response to radiation may lead to position changes of the triplets in DNA molecules, resulting in coding errors for protein building. Such changes can lead to diseases of genetic origin.

The radio-induced structural alteration of the nucleic acid has a lethal effect on the cell when the cell loses its ability to divide. This occurs because of an irreparable impairment of hereditary information encoded in the nucleotide sequence of the DNA. It can occur through three main mechanisms:

- breaking of the main chain;
- intramolecular bridges formation (covalent bonds, cross-link) that block the duplication process, preventing the separation of the two strands of the nucleic acid;
- structural modification of purine and pyrimidine bases. This can lead to a gene mutation of greater or lesser gravity in function of the character coded by the gene involved.

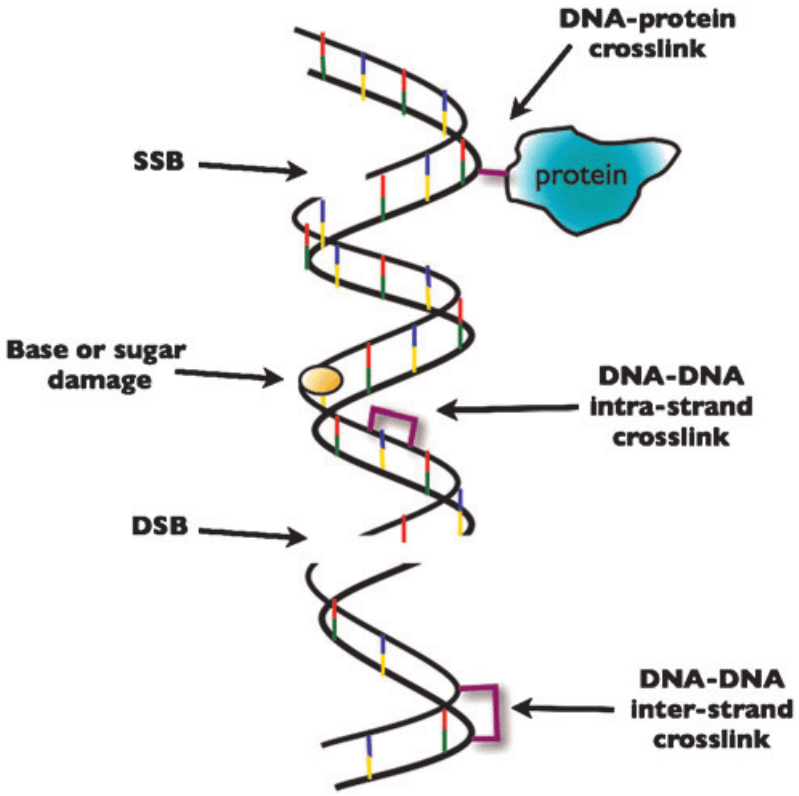

Figure 1.3: Principal DNA damage types induced by ionizing radiation. [43]

The breaking of a single chain occurs when damage to one of the two chains leaves the complementary strand intact. The repair mechanism of this kind of damage is quite simple: the section of the chain containing the breakage is removed and then rebuilt employing the complementary chain as a reference and finally reconnected by an enzyme called ligase. The number of single strand break has been shown to be linearly related to the dose of radiation within a very wide range. The average energy required to produce a single break is comprised between 10 and 20 eV in the case of weakly ionizing radiation.

The breaking of the double chain occurs when two breakages on individual adjacent chains cause the detachment of part of the DNA. A double breakage can derive either from ionizing events due to the same radiation, affecting two chains simultaneously or from the combination of two events due to different single breaking events which, incidentally, affect two nearby points of two chains of the same macromolecule. The former happens especially with highly ionizing radiation; in fact, the high density of the delivered dose makes a double breaking event quite probable. The latter occurs when the second radiation damage is dealt before the first can be repaired. This most likely occurs in the presence of a high dose rate. The relationship between dose and number of double breakage has been experimentally sought; the model more accepted is the linear quadratic. It seems that a double chain breaking cannot be repaired or possibly can be repaired by an "error-prone" mechanism.

1.4.2 Cell survival curves

After a single dose of ionizing radiation, the number of living cells (surviving fraction) decreases with increasing dose. The graphic expression of this phenomenon is the cell survival curve.

The typical survival curve for mammalian cells has a "shoulder" at low doses and becomes exponential only for higher doses. The parameter D_0 determines the slope of the linear part of the curve and indicates the dose which reduces the surviving fraction to a

factor equal to 0.37. The number of extrapolation N, which is obtained by extrapolating the linear portion of the curve until it intersects the y-axis, is an index of the cell's ability to store and repair the sublethal damage and it represents the number of targets to hit to produce cell death. Typically D_0 has values between 1-2 Gy and N between 1 and 5. The width of the shoulder is indicated by a parameter D_q (quasi-threshold dose), which is the intersection between the extrapolation of the straight portion of the curve and the horizontal line passing through the 100% of survival.

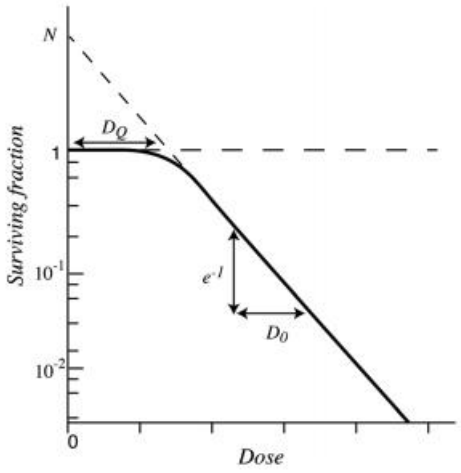

Figure 1.4: Cell surviving fraction as a function of dose. It clearly shows the initial shoulder [42].

To interpret the behavior of survival curves in which a shoulder is present, a theoretical model was developed based on the assumption that inactivation of a cell requires the inactivation inside the cell of a number $n \geq 1$ of targets, each of which requires a single shot to be inactivated (hypothesis of multiple targets single-shot). The inactivaction of the cell occurs only when a number of a sublethal events occur within a short period of time. At low dose, only a few events per cell will occur, thus making cell death unlikely. There will be a dose range in which inactivation is not experienced (part of the shoulder). At higher doses, interaction events within cells begin to add up, until the first

inactivations occur, the survival curve will begin to trend downward (passage between the shoulder and linear region). Increasing the dose further, the number of events per cell will keep growing, tending to be n-1 in each of them. Above this dose the behavior is identical to a system of elements inactivable with a single hit, since a single additional event per cell will reach the N threshold and will cause inactivation.

The analytical expression corresponding to this theoretical model is the following:

$$f = 1 - (1 - e^{-\frac{D}{D_0}})^N \tag{1.6}$$

This model implies a zero slope at very low doses, but experimental data are often not in agreement with it. It is possible to modify the simple multitarget model to improve the shape of the curve in the low-dose region, by ,ultiplying the multitarget term by a single-target term (two component model), obtaining the following analytical expression:

$$f = e^{-\frac{D}{D_1}}[1 - (1 - e^{-\frac{D}{D_2}})^n] \tag{1.7}$$

A model widely used in radiotherapy is the linear quadratic, where the fraction of surviving cells is:

$$f = e^{-(\alpha D + \beta D^2)} \tag{1.8}$$

D is the dose, α and β are two costants that mean:

- α: log of cells killed per Gy, is the constant of proportionality linearly linking the cellular lethality to single hit damage;
- β: log of cells killed per Gy^2, is the constant of proportionality quadratically linking the cellular lethality to damage due to the sum of sub-lethal events.

The ratio α/β is the dose in Gy at which lethality is equally likely to be due to a single events and to an accumulation of sublethal damage.

The component αD represents a non-repairable damage (the dose/effect relationship is linear, from a single shot, and therefore even small doses are able to cause damage),

while the component βD^2 indicates the existence of recovery process (more hit events), the dose should increase quadratically to surmount them.

In the case of fractionated irradiation, figure 1.5, at each subsequent irradiation reoccurs the shoulder, because of the repair of sublethal damage by the elements of the system. The overall dose, necessary to obtain the same degree of cell inactivation, must be increased by D_q times the number of fractions -1. The fractionation of dose in radiotherapy involves a "therapeutic gain", in fact, it increases tollerance in normal tissue (due to repair of damage induced by radiation) and, at the same, time eliminates the radioprotective effects of hypoxia on tumor (due to reoxygenation phenomena).

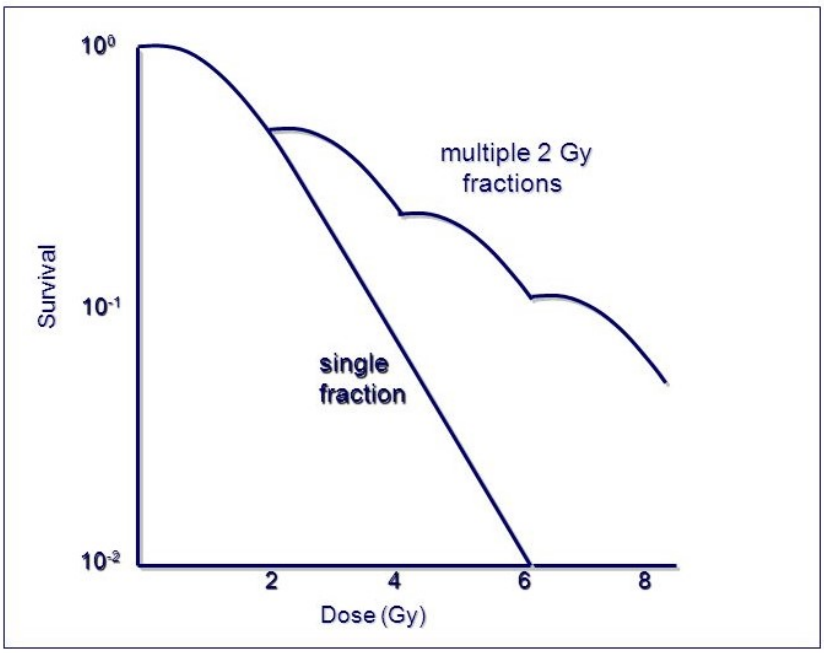

Figure 1.5: Fractionated irradiation: the overall dose is given by $D_f = D_u + (n-1)D_q$, where n is the number of fractions.

1.4.3 Radiation quality

Although all ionizing radiations interact with living matter in a similar manner, different types of radiation differ in their effectiveness, or ability to do harm to a biological system. The various radiations, in fact, interact with matter in a different way in relation to the amount of energy deposited along their path.

The transfer of energy of radiation is defined by LET (linear energy transfer) and denoted by the symbol L_Δ, [3]

$$L_\Delta = \left(\frac{dE}{dl}\right)_\Delta$$

where dE is the local energy loss due to collisions for a charged particle along a track segment dl, considering only collisions involving transfer of energy less than $\Delta(ineV)$.L_Δ is abitually expressed in $KeV \cdot \mu m^{-1}$, if $\Delta = \infty$ all energy losses are considered. High LET means high specific ionization, and is not connected to the energy because some particles can have an high LET at low energy and a low LET at high energy.

- Low-LET radiations have a track with primary events (collisions) well separated in space; it is the case of X-rays which are said to be sparsely ionizing;
- High-LET radiations have tracks with primary events very close in space. It is the case of ions and heavy particles which are said to be densely ionizing.

A different LET leads, at equal doses, to different biological effects and in order to take this fact into account the Relative Biological Effectiveness, RBE, has been introduced. The intent is to quantify the effect, at the same imparted dose, of radiation r in comparison with reference radiation which is assumed to be X-rays at 250 KeV. By this definition, the reference radiation has RBE equal to 1; this way it, quantifies the increment of biological effects of highly ionizing radiations with respect to X-rays at the same physical dose.

Its follows: the RBE of some test radiation (r) compared with X-rays is defined by

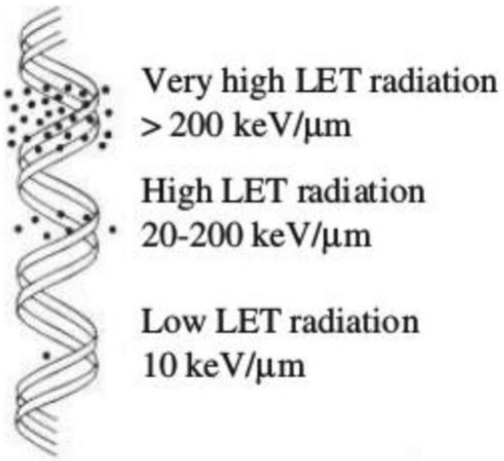

Figure 1.6: Comparison of ionization density depending on radiation LET [42].

the ratio [7]

$$RBE = \frac{D_{250}}{D_r}$$

where D_{250} and D_r are respectively, the doses of 250 KeV X-rays, and of the test radiation required for the equal biological effect. The higher the LET, the higher the RBE, as it is shown in figure 1.7 for radiation of different LET. RBE increases with increasing LEt up to a certain maximum. If the LET is further increased, far fewer tracks are required to deposit the same dose, leading to saturation of the effect and eventually to decrease of RBE with increasing LET [8].

Since prescribed doses to the target, dose constraints to critical structures and fractionation schemes are largely based on clinical experience gained with photon therapy, prescription doses for proton therapy are also defined as photon doses. Therefore, the RBE adjusted dose has been introduced, defined as the product of the physical dose and the respective RBE. Before 2008 proton doses were given in Cobalt Gray Equivalent (CGE), and then it was changed to reporting D_{RBE} as Gy(RBE) [9]. Most proton therapy treatment facilities have adopted a generic RBE of 1.1. This value is mainly based on animal experiments performed in the early days of proton therapy [10] However, dif-

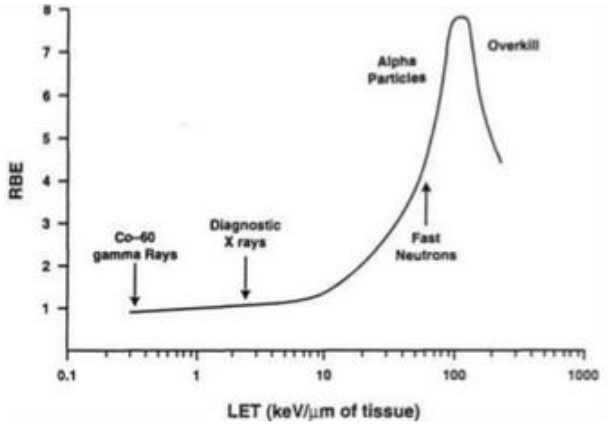

Figure 1.7: LET at which the RBE reaches a peak is the same (about 100 $KeV/\mu m$) for a wide range of mammalian cells, as the LET increases, RBE increases slowly at first and then more rapidly, with LET level beyond 10 $KeV/\mu m$. Over 100 $KeV/\mu m$, the RBE again falls to lower values, as the densely ionizing radiations produce easily and often a DSB, but energy is "wasted" because ionization events are too close together and produce an overkill effect.

ferences in biologcal effect occur not only between X-rays and protons, but also between protons at different energies, as well as depth of penetration, biological endpoint, dose per fraction, position in the SOBP and particulr tissue. nevertheless, there are no clinical data indicating that the use of a generic RBE of 1.1 is unreasonable.

1.5 Accelerator

The instrument used in proton therapy is mostly the same that are used for nuclear physics: accelerators, detectors and Monte-Carlo simulation. A particle accelerator is a machine that aims to produce ions or particles beam at high energy. There are two principal kinds of accelerators: cyclotrons and synchrotrons. In this thesis only cyclotron will be taken into account, because at the moment it is the only accelerator used in proton therapy.

1.5.1 Cyclotron

The cyclotron is a kind of particle accelerator, developed by Ernest Lawrence in 1932, where charged particles are accelerated from the center to the external part following a spiral path. The trajectory is induced by a static magnetic field and the particles are accelerated by an oscillating electric field.

The idea is to make protons circulate inside two hollow electrodes, one with a "C" shape and the other with a "D" shape, both inserted between two poles of a magnet. A representation of a cyclotron is visble in Figure 1.8. Every half round protons are

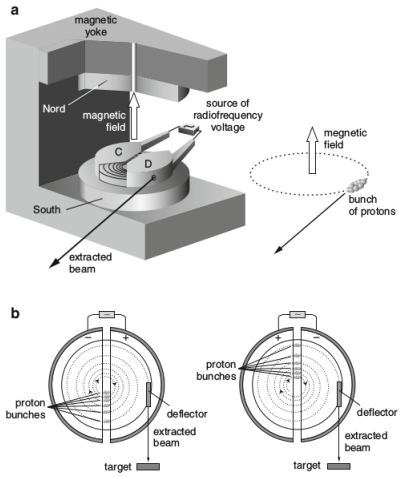

Figure 1.8: Structure of a cyclotron and path of protons inside it.

accelerated by the alternating voltage applied between the electrodes: thanks to the combination of an electric and a magnetic field (acceleration and deflection), the proton beam will follow a spiral trajectory. The main advantage of this accelerator is that it permits to reach higher energies with a smaller machine and with lower tension compared to normal electrostatic accelerator.

Protons are inserted exactly at the center of the cyclotron at low energies and gaseous hydrogen ionized by an electric discharge is used as source. As said before the energy of proton beam will increase every half loop, as it will encounter on a potential difference

between the two electrodes that will accelerate it, this potential difference will be flipped when protons will be again close to the next half loop so that they will increase energy again. To extract the protons there will be a deflector that will permit the beam to proceed out on a line, creating the real beam [11].

Equations that regulate how cyclotrons work are well known: F_C the centripic force, for non-relativistic particles, necessary to keep them in a circular orbit is:

$$F_C = \frac{mv^2}{r}$$

where m is the mass of the particle, v it's velocity and r the radius of the trajectory. This force is due to Lorentz's force $f - b$ of the magnetic field B:

$$F_B = qvB$$

with q that is the charge of the particle. The maximum energy is reached at the extremity of the electrodes, where the radius is $r = R$ (R is the radius of the electrodes). Combining the two forces and knowing that the kinetic energy is: $K = \frac{1}{2}mv^2$ is it easy to find that the kinetic energy of the beam is:

$$K = \frac{q^2B^2R^2}{2m}.$$

Alternating voltage frequency depends on the cyclotron's resonance frequency ν that is

$$\nu = \frac{qB}{2\pi m}.$$

Important evidence emerging by the last equation is the independence of ν by the radius. This behaviour is true when we deal with a non-relativist particles speed.W when the ratio $\beta = v/c$ start to grow we have to consider that mass is no more constant, but it became the relativistic mass

$$m = \frac{m_0}{\sqrt{1-\beta^2}} = \gamma m_0$$

γ is called relativist factor and is shown in Figure 1.9. Therefore the new frequency of resonance will now depends also on the speed of the particle:

$$\nu = \frac{\nu_0}{\gamma} = \nu_0\sqrt{1-\beta^2}.$$

This effect is not negligible for proton therapy, because for deep tumors protons used have energy around 200 MeV to which correspond $\beta = 0.55$. Cyclotrons that consider this correction are called synchrocyclotrons.

The beam produced by a cyclotron has always the same energy, that is, in therapeutic cases, approximately 230-250 MeV, and a fixed frequency of pulsation, around 10-20 ns. An Energy Selection System reduces the energy through the insertion of some absorber, to reach the energies necessary to hit target always less deep (it requires generally between 50 and 100 ms). The interaction between the beam and the absorbers produce nuclear reactions that generate a radioactive area around the patient, especially if the energy has to be reduced a lot.

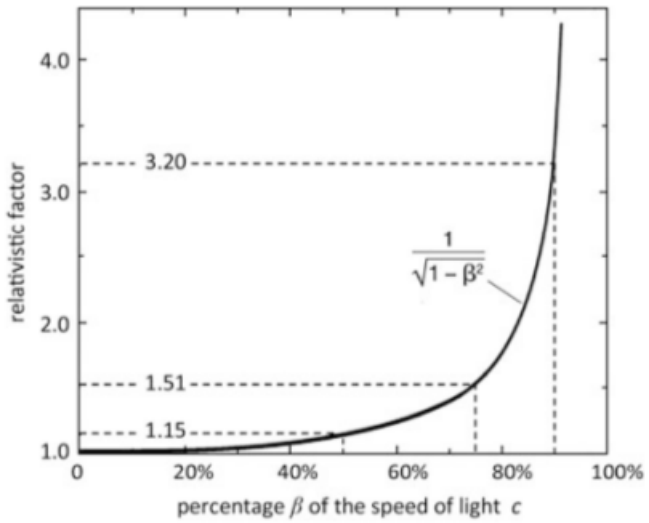

Figure 1.9: γ in function of β.

Chapter 2

PSI status and planning dose

2.1 PSI facilities

The Center for Proton Therapy (CPT) at Paul Scherrer Institut (PSI) is in operation since 1984, with more than 8000 patients treated. Furthermore, since 1996 the center introduced the pencil-beam scanning technique for treating large and deep seated tumors, as for example chordoma and chondrosarcoma of the skull base or along the spinal cord. In fact, PSI has developed the worldwide first compact scanning gantry for the irradiation of deep seated tumors with proton beam.

The entire proton delivery ficility is shown in Figure 2.1. The Core of the facility is COMET, a 250 MeV superconducting cyclotron where the protons are accelerated. The beam is then deflected by means of electromagnetic switches to one of the four therapy stations (Gantry 1, Gantry 2, Gantry 3 and OPTIS 2), within less than a thousandth of a second. Hardware and software for control and safety systems of Gantry 1, Gantry 2 and OPTIS 2 have been completely developed at PSI. Gantry 3, that has same capabilities as Gantry 2 on a technical level, has started treatments in June of 2018 and was developed by Varian, as well as the software to use this gantry.

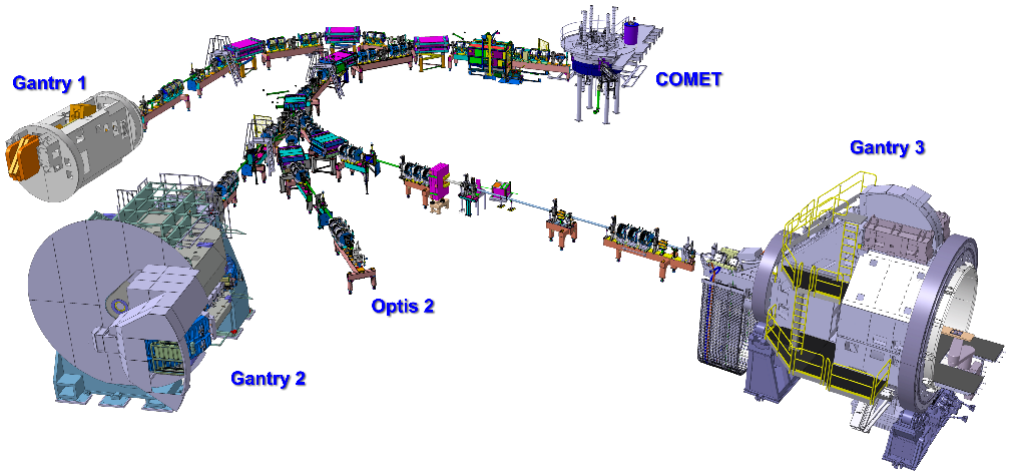

Figure 2.1: Illustration of the facility for proton treatment at CPT, in PSI: the cyclotron COMET, OPTIS 2, Gantry 1, Gantry2 and Gantry 3 [26].

2.1.1 OPTIS 2

OPTIS 2 (figure 2.2) is dedicated to treatment of ocular tumors using the passive scattering technique with a fixed horizontal beamline. It is a newer and more advanced version of its ancestor facility, OPTIS 1, that has been in operation from 1984 to 2010.

The patient is seated in a treatment chair facing the nozzle with head immobilized using an individualized mask and a bite block. The chair is mounted on a hexapod robot allowing the positioning of the patient with 6 degrees of freedom. For allowing the localization of the tumor during the treatment with sub-millimeter accuracy, several small clips are suturated on the sclera (eye surface) in the proximity of the target during a previous surgical operation. For positioning the patient in the most accurate way, OPTIS 2 uses two X-rays, aligned with the treatment isocenter so to provide orthogonal images of the eyes of the patient. The patient has to fix a LED light throughout the treatment, whose position is optimized at the time of planning as a compromise between patient comfort and best entrance direction of the beam, in order to cover in the best way the extension of the tumor, while sparing as much as possible eyelid and pupil.

Intrafractional motion of patient eye is monitored using beam's eyes view camera.

As eye tumor is shallow the energy used for this type of tumor is 70 MeV. However, during the energy degradation from 250 MeV (energy given by cyclotron) more than 99% of the original protons is lost. For that reason, in order to ensure a higher efficiency of transport, a double-scattering process is implemented in OPTIS 2. The extracted beam passes through a range shifter, used for setting the range and ensuring pre-scattering of proton pencil beam and ensures homogeneous field at isocenter. Depending on the needed ranges, 9 scatter foils are available. The Spread-Out Bragg Peak is then realized using dedicated modulator wheels. The maximal diameter of the circular field is 35 mm, reduced for each patient using individually milled copped collimator aperture.

Figure 2.2: OPTIS 2 Facility at PSI [26].

2.1.2 Gantry 1

Gantry 1 (figure 2.3) is the first facility worldwide that used active scanning technique for treatments of deep-seated tumors. It has been operational from 1997 until January of 2019, treating tumors located mainly in the skull, spinal cord and in the pelvis. Future of this gantry is still under decision and it will be probably used for biological and clinical

research.

The transverse movements of the pencil beam are done with a fast scanning magnet and patient-table motion respectively, while the third dimension (depth) is varied adjusting the beam range. To do that, 40 range-shifter plates of polyethylene are placed into the beam path by means of a pneumatic system, at the nozzle level. To ensure quality and safety of delivery, the beam is monitored in the nozzle using two plane-parallel ionization chambers for checking the dose, a strip chamber for controlling in two dimensions position and width of the beam.

The weak points of Gantry 1 were [12] :

- the unsatisfactory access to the patient table when the beam is applied from below;
- the slow speed of scanning, that is a limitation for applying repeatedly target repainting and, this makes the treatment of moving organs not really possible on this gantry.

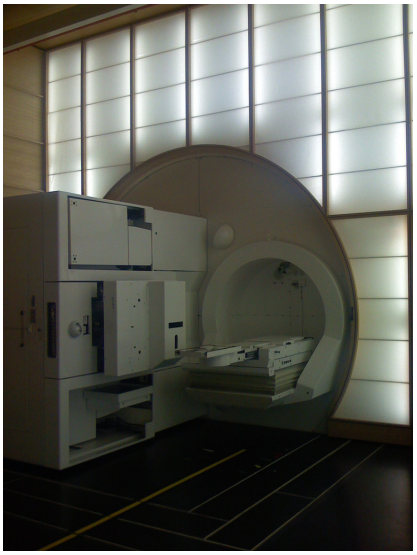

Figure 2.3: Gantry 1 Facility at PSI [26].

2.1.3 Gantry 2

The positive experience of using the scanning technique brought in the year 2000 the decision of PSI to expand and upgrade the facility. It is in the frame of this new project, called PROSCAN, that the realization of Gantry 2 was planned. Treatment in this gantry (Figure 2.4) started in 2013. The design of the Gantry 2 is derived from the practical experience of using Gantry 1, but is substantially improved and renewed.

For what concerns the layout, Gantry 2 has a larger diameter, of 7.5 m (isocentric), compared to the 5 m (eccentric) of Gantry 1.

The major improvement concern the speed of the beam delivery. In fact two high-speed magnets (scanning speeds of 2 cm/ms and 0.5 cm/ms for the two axes) are used to scan through the tumor in two dimensions. This double scanning and the isocentric layout permit comfortably large space around the couch, thus fast and easy access to the patient table. The depth of penetration of the protons can change from one tumor layer to the next one in about 100 ms (80 ms for 3 MeV energy changes). That approach permits to generate dose distributions less sensitive to organ motion and allows to implement repainting. Moreover, on this machine both discrete and continuous line scanning can be applied [13]. However, for now, only the discrete approach is used on patients.

In addition, the components in the nozzle are designed to have as little materials as possible along the beam path. This maintains a small spot size at all energies (width lower than 4 mm for 100-230 MeV). The nozzle can be also extended to reduce the air gap between the beam line exit window and the patient, mitigating in this way the angular spread of protons. An electronically controlled range-shifter of 4 cm water-equivalent thickness is mounted within the nozzle and can be remotely positioned into the beam to allow the delivery of Bragg peaks close to the patients surface (proton's energy lower than 70 MeV) [14].

Further notable development is the in-room imaging: a sliding CT scanner, used for treatment planning and for the daily verification of the patient position. This allows

to reach the CT in a single movement of the patient table. Moreover, another X-ray system is mounted on the gantry itself, which takes images in the direction of the proton beam, the so called "beam's eye view". Thanks to its fluoroscopy capability, it provides increased precision and quality assurance, in particular in the treatment of moving tumors.

Figure 2.4: Gantry 2 Facility at PSI, the picture includes also the dedicated CT scanner. [27].

2.1.4 Gantry 3

The gantry design is based on Varian technology, which has been combined with advanced PSI active scanning technology. In fact a major challenge with gantry 3 was the link of the existing PSI PROSCAN system with the Varian ProBeam system, while retaining the system integrity and high performance level. An additional problem was the installation and commission of Gantry 3 while keeping the other treatment room in full operation.

Mechanically, Gantry 3 is an implementation of the ProBeam Gantry by Varian [15]. It rotates over 360° and has a total weight of 270t. The rotating parts have an envelope diameter of 10.5 m and a length of 10 m. The beam is deflected from rotational axis by 45° dipole and bent towards the iso-center through a 135° dipole. Five quadrupoles and three

Energy range	70-230 MeV
Energy precision	< 0.1 MeV
Beam momentum spread	< 1 %
Layer switching time	200 ms
Beam FWHM at IC (in air)	8.5 mm
Lateral beam position precision Iso-Center (IC)	1 mm
Field size	300 x 400 mm^2
Dose delivery	2 Gy/liter/min

Table 2.1: Gantry 3 Main Performance Specification [16]

orbit correction magnets are used to set the beam optics. Two additional quadrupoles have been introduced at the entrance to the Gantry in order to facilitate beam matching between PSI and VMS beamlines and to enhance the transmission through the Gantry beam transport system.

Gantry 3 is a downstream, divergent raster scanning system. The scanning magnets are placed after the last 135° dipole and allow a maximum field of sized 30 x 40 cm.

One major goal for Gantry 3 was to achieve overall system performance comparable to Gantry 2. Table 2.1 lists the main performance parameters of Gantry 3. One of the main development achieved thanks to the collaboration with Varian has been an energy layer switching time of 200 ms; it includes modifications on the beamline hardware as well as adaptations and new developments on the control system side.

Gantry 3 has been equipped with a 360° co-rotating X-ray system. A further development was the upgrade of the X-ray system to a cone beam CT (CBCT). Gantry 3 is shown in Figure 2.5. The first patient has been treated in June 2018 and the gantry is actually perfectly working at full capacity.

Figure 2.5: Gantry 3 Facility at PSI [26].

2.1.5 COMET

In May 2001, PSI signed a contract for the delivery of a new cyclotron, named COMET, Figure 2.6). It is based on a design of Blosser, NSCL, (USA) and has been manufactured by ACCEL Instruments GmbH (D), in close collaboration with PSI. The cyclotron has been delivered in March 2004 and the first beam was extracted one year later. After a period of machine tuning, commissioning and acceptance tests, the cyclotron has been accepted by PSI in 2006.

The cyclotron accelerates protons to a fixed energy of 250 MeV. The 3.8 T magnetic field is provided by super conducting coils. The high extraction efficiency of at least 80% [17] is an important routinely fulfilled specification that has never been achieved before in compact cyclotron of this energy. This minimizes the amount of radioactivity in the machine and thus allows a relatively short waiting time for service. At PSI rigorous beam dynamics calculations have been performed during design phase, to study the effect of possible misalignments of magnetic coils and the effect of betatron resonances on beam losses [18]. These studies were very helpful to understand and minimize the beam losses observed in the start up phase. Afterwards, work focused on increasing the degree of automation of the control system and on improving of the stabilization of the beam intensity in the kHz range.

Figure 2.6: A view of the cyclotron COMET used at Paul Scherrer Institute [26]

2.2 Planning dose

Proton therapy provides a tool for delivering highly conformal dose distributions, since protons show the attractive physical characteristic of having a well-defined range, beyond which no energy is deposited. However, the resulting proton dose distribution is strictly related to the technique used for the delivery, as well as the type of treatment plan defined on the patient.

2.2.1 Beam delivery systems

After the protons have been accelerated, either by a cyclotron or a synchrotron, they are transported into the treatment room through the beam line. The output proton beam is mono-energetic with a diameter of only few millimeters. Clinical use of the proton beam requires both spreading the particles to a useful uniform area in the lateral direction, as

well as creating a uniform dose distribution in the depth direction. The main function of the treatment head, also called nozzle, is shaping the proton beam into a clinically useful 3D dose distribution [3]. Two modalities of beam spreading are used: passive scattering [19] and active scanning [20] (see Figure 2.7). With the last approach, the full potential of protons can be exploited as the Bragg peaks can be deposited anywhere in three dimensions within the tumor volume.

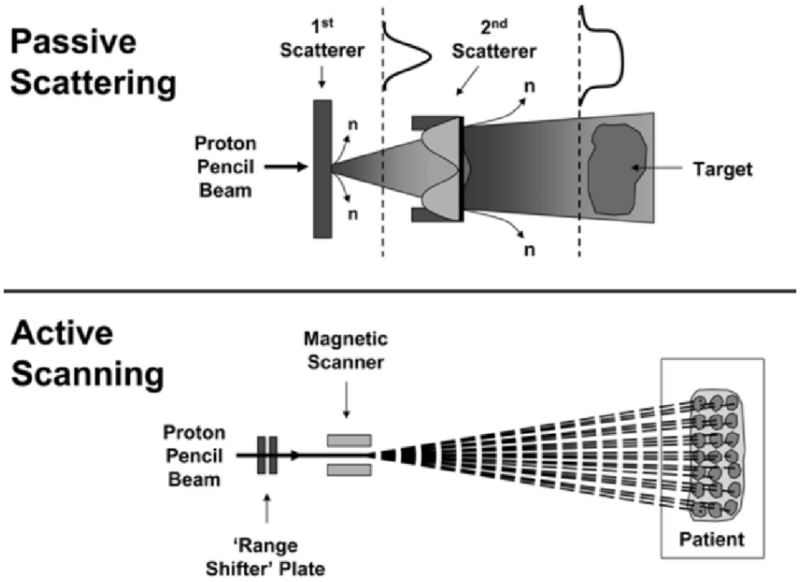

Figure 2.7: Schematic diagrams of passive scattering and active scanning techniques [28].

Passive scattering

Passive scattering is a delivery technique in which range shifting and scattering materials spread the proton beam.

In order to have a uniform dose region the depth direction, Bragg peaks are shifted in depth and given appropriate weight, so that a Spread Out Bragg Peak (SOBP) is created by combining these proton beams of decreasing energy. This method of adding pristine peaks is called "range modulation". Depending on the size of the target to be

covered, the extent can be adjusted by changing the number of peaks. There are three principal range modulation techniques:

- Energy stacking: it is the easiest method because no dedicated nozzle elements are required since the energy of the protons is changed at the accelerator level. This can be achieved either by changing the extracted synchrotron energy or the energy-selection system setting at the exit of the cyclotron.

- Range modulator wheels: this method has been proposed by Wilson in his original article about proton therapy [1] and continues nowadays to be the most common approach in clinical proton-scattering systems. A range modulator wheel has steps of varying thickness and a certain angular frequency. Each step corresponds to a certain Bragg peak, that is irradiated sequentially during the rotation. The thickness of a step determines the range shift of the related pristine peak, while its angular width affects the number of protons hitting the step, thus the weight of the peak.

- Ridge filters: it is a stationary device composed of tens of bars, where each bar has the same ridge shape. The range of protons in a spot is modulated according to the position they pass through, resulting in the broadening of the Bragg-peaks. The principle is the same as the modulator wheel: thickness and width of the steps determine respectively the range and the weight of the peaks.

The uniformity of the dose along the lateral dimensions is instead achieved thank to designed specifically scatters. The simplest scattering system is a single, flat scatterer that spreads a small proton beam into a Gaussian-like profile. Typically the scatters are high-Z materials, e.g. lead and tantalum, providing the largest amount of scattering for the lowest energy loss. Due to its low efficiency, defined as the portion of protons inside a useful radius, this approach is limited to small fields with a diameter lower than 7 cm [3]. To overcome this limitation, a double scattering system can be used to scatter more of

the central protons to the outside and create a flat profile. Usually a flat scatterer spreads the beam onto a contoured one, so that the profile is flattened at some distance. Since this contoured scattered is thick in the center and thin on the outside, protons hitting the center lose more energy than those going through the periphery. For that reason, normally the high-Z scattering material is combined with low-Z compensation material, e.g. plastic, with thickness designed to provide constant energy loss, while maintaining the appropriate scattering power variation. Hence, the thickness of scatterer decreases with distance from the axis, whereas for compensation material the thickness increases. If the energy compensated contoured scatterer is used, the energy of the protons needs to be increased in order to achieve the same range in the patient as with an uncompensated scatterer.

Finally, to confirm the dose to the target, field-specific apertures and range compensators are used. The first ones block the beam outside the target and adjust the beam laterally, while the compensator is a variable range shifter that conforms the beam to the distal end of the target. This conformity is in 2D, as the SOBP is constant and equal to the maximum required to cover PTV.

Active scanning

The principle of active scanning proton therapy have been first proposed by Kenai et al. in 1980 [21] and is strictly connected to the fact that protons are charged particles, thus can be deflected by magnetic fields. This approach was clinically implemented first at PSI, where patients have been treated since 1996 on a fully rotational treatment gantry [22]. In active scanning, also called Pencil Beam Scanning (PBS), the beam transported to the nozzle is directly sent to the patient without interacting with any scattering or energy-modulation devices. Active Scanning has proven to be very good for clinical treatment as it modulates the dose in 3D, also proximal to the tumor, and not in 2D as for passive scattering.

This technique consists of the superposition of individual Bragg peaks positioned in 3 dimensions inside the tumor's volume. The 3D allocation of these peaks is in general performed thanks to sweep magnets. However, the mechanical configuration can be different depending on the gantry. The first one uses one sweep magnet only and the movement of the couch, while the latter one exploits magnets along 2 dimensions. The third dimension is instead covered by changing the energy of the beam. For a synchrotron it can be simply varied changing the applied fields, while in case the accelerator is a cyclotron a degrader at the exit must be used. Moreover, range-shifter within the nozzle allows the delivery of Bragg peaks close to the patient surface. This expedient is introduced in order to have a proton beam with sufficient intensity, condition unreachable using the degrader only.

In traditional active scanning, namely discrete spot scanning, the dose is applied in discrete steps both laterally and in depth, with each position typically being called a spot. When the beam is on this spot is static and, after each spot, the beam is switched off and the magnetic and/or energy settings are changed to move to the next spot. The time required for these changes is called dead time. As a consequence of this, the total treatment time is substantially longer than the actual beam-on time, in which dose is delivered. A reduction in dead time can be achieved by scanning the beam continuously, at least along one of the axes in lateral plane. This concept leads to another modality of PBS, called continuous line scanning. By modulating the scanning speed and the beam intensity, it is possible to apply almost arbitrarily complex, inhomogeneous proton fluences along each line. In this mode, position and dose checks are either performed during irradiation, after scanning a single line or after each isoenergy layer. Continuous line scanning can be considered as a superposition of an infinite number of spots on a scanning grid with an infinitesimal spacing [13].

2.2.2 Treatment plans

Typically, two major categories of plans can be delivered, namely Single Field Uniform Dose (SFUD) and Intensity Modulated Proton Therapy (IMPT) plans [23] [24]. The first method can be delivered with passive scattering as well as by means of pencil beam scanning, while IMPT is restricted to active scanning only.

For both SFUD and IMPT with PBS, the treatment planning system considers pencil beam Bragg peak explicitly, rather than their combinations of any type as for scattering, and the quality of the beam is determined largely by the quality of the individual pencil beam [23]. The specification of treatment beam is basically a list of Bragg peaks, each with the energy of the protons, the lateral location of the peak projected onto the isocenter plane, and the number of protons often given in the unit of Giga-protons [3].

SFUD plans

In treatment planning of proton therapy for Single Field Uniform Dose, each field is composed of different Bragg peaks with weights optimized in such a way that the single field dose distribution in the target is homogeneous. The plan is obtained by a linear combination of individually optimized fields, which improves the dose homogeneity in the tumor, while distributing the entrance dose on a larger surface (Figure 2.8).

This approach essential arises from passive scattering delivery, since also in this case the delivered SOBP applies a uniform dose across the target. However, there are few notable differences in particular the active scanning approach adds some flexibility, allowing both distal and proximal conformity for a single beam, thanks to the fact that range and modulation width are set on a per-proton-ray-beam basis [3]. For this reason, SFUD with active scanning can be considered more efficient as only Bragg peaks are delivered within, or close to, the target [25].

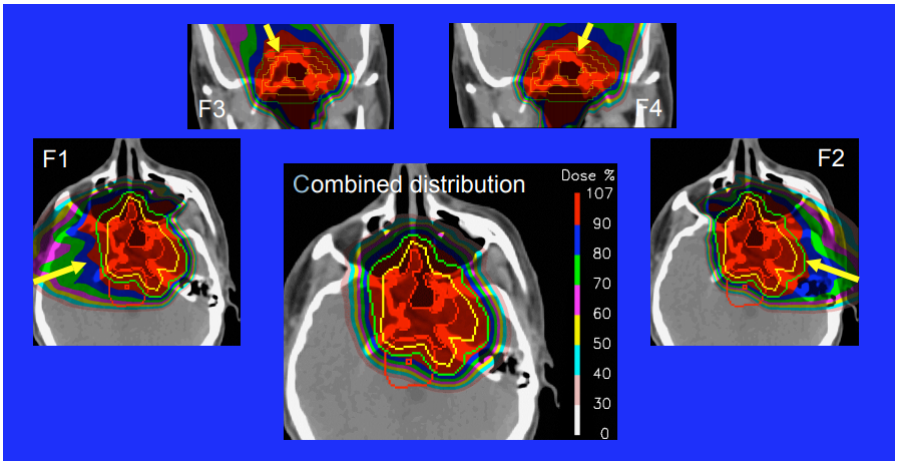

Figure 2.8: Example of SFUD plan. The critical structure is contoured in red. Picture taken from A.J. Lomax PTCOIG teaching course.

IMPT plans

In treatment planning of proton therapy for Intensity Modulated Proton Therapy, also called Multi-Field Optimization (MFO), the desired coverage of the target with homogeneous dose is achieved only by combination of two or more treatment fields, each of which can deliver a highly inhomogeneous dose distribution to the target (figure 2.9). The resulting plan is given by the simultaneous optimization of all Bragg peaks from all fields.

With this technique, the weight of the spots is optimized taking into account also the dose to healthy tissue and Organs At Risk (OAR) close to or embedded in the target. Depending on the anatomy and field direction, certain parts of the target can be irradiated only by certain fields. Moreover, another difference in this approach is that the uniform single field constraint is removed and to the optimizer is given full reign to weight Bragg peaks regardless of the final shape of the individual field dose distribution, as long as the total dose, sum of all the individual field dose distributions, gives the desired result. For these reasons, the IMPT approach best exploits the full potential of scanned proton therapy, in fact it provides even more flexibility in tailoring the dose

distribution to the target and in selectively avoiding critical structure [25].

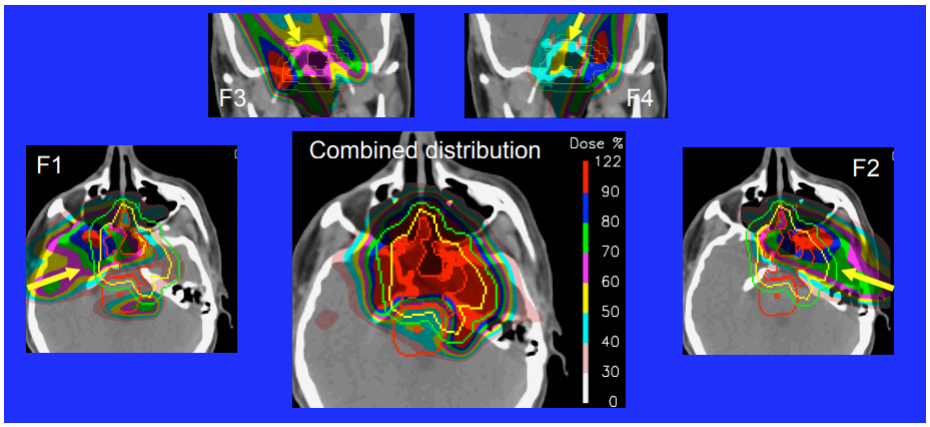

Figure 2.9: Example of IMPT plan. The critical structure is contoured in red. Picture taken from A.J. Lomax PTCOIG teaching course.

2.3 4D theory

Anatomy can change significantly with time both during and between radiation treatments. Intrafraction anatomic motion deformations occur because of the respiratory, digestive and cardiac systems. Interfraction motion and deformation occur because of tumor shrinkage or growth, translations and rotations of the target within the skeletal anatomy. These temporal anatomic changes are not explicitly accounted for with standard conformal proton therapy or IMPT approaches. Moreover, imaging, planning and delivery errors can be introduced by not explicitly accounting for respiratory motion.

If respiratory motion is not accounted for during computed tomography image acquisition as is the case when conventional proton therapy techniques are applied in thoracic and abdominal sites, this motion causes artifacts during image acquisition. These artifacts cause distortion of the target volume and incorrect positional and volumetric information [29].

During treatment planning margins need to be large enough to ensure coverage of the target at the full extents of motion. Generally, for CT-planned lung cancer treatments, the Gross Tumor Volume (GTV) is outlined, from which a margin is added to include the suspected microscopic spread (which added to the GTV creates the so-called Clinical Target Volume (CTV)). Obtaining the Planning Target Volume (PTV) from the CTV involves the addition of the internal margin and the setup uncertainty margin. The internal margin by definition includes both intrafraction (because of respiration) and interfraction motion. Accounting for respiratory motion adding treatment margins to cover the limits of motion of the tumor is clearly undesirable because this increases the volume of healthy tissues exposed to high dose. This increased treated volume increases the likelihood of treatment-related complications. However, if the margins are not sufficiently large, part of the CTV will not receive adequate dose coverage.

A method to alleviate the respiratory motion problems is to use 4-dimensional (4D) or tumor tracking proton therapy. 4D proton-therapy can be defined as "the explicit inclusion of temporal changes in anatomy during imaging, planning and delivery of proton therapy". Note that this covers both intrafraction and interfraction motion issues.

In principle, 4D proton therapy is intuitive and simple. However, in practice, 4D proton therapy is a very difficult problem, with many levels of complexity. It will be discussed later the aspects of imaging and planning in 4D therapy. It is important to note that respiratory gating and breath hold techniques can achieve same goals as 4D proton therapy [30] [31].

2.3.1 Rationale for 4D proton therapy

Lung cancer has a poor prognosis. The estimated 5-year survival for lung cancer patients is 15% [32]. However, there is strong clinical evidence that higher tumor doses result in a survival advantage for lung cancer patients and also that lower lung doses result in reduced lung complications as expanded on later.

Thus, there is clinical evidence that technologies, such as 4D proton therapy, which through safe PTV volume reduction will allow an increased dose to the tumor while sparing healthy tissue can improve balance between complications and cure.

2.3.2 4D CT Imaging

The advantage of 4D over 3D CT imaging is that not only the motion artifacts are reduced, but the tumor and organ motion information is also encoded in the 4D image set. [33] A schematic diagram of the 4DCT image acquisition and planning process is shown in Figure 2.10.

The patient is CT scanned using a spiral technique. As the patient is scanned, the respiration signal is simultaneously acquired. Once the images are acquired, they are postprocessed into individual 3D image sets according to the respiratory phase at the time each image was acquired. Because many 3D CT scan sets constitute a 4D scan, more slices are necessarily acquired. This increase in the number of slices raises issues with patient dose, CT tube heating and data management.

Breath should be as much as possible regular. Irregular respiration, particularly variations in amplitude between breathing cycles, makes the acquisition of high-quality 4DCT extremely difficult.

Rather than sorting images into their respective phase bins, retrospective image reconstruction techniques, which operate in sinogram space rather than image space, allow improved temporal resolution for 4DCT. A technique that is emerging in these years is 4D cone beam CT, that allows a full thoracic CT scan to be performed in only a few respiratory cycles. Another interesting future development is combined 4DCT/Positron Emission Tomography (PET). The combination of 4DCT with 4DPET holds significant promise for lung cancer proton therapy imaging and treatment.

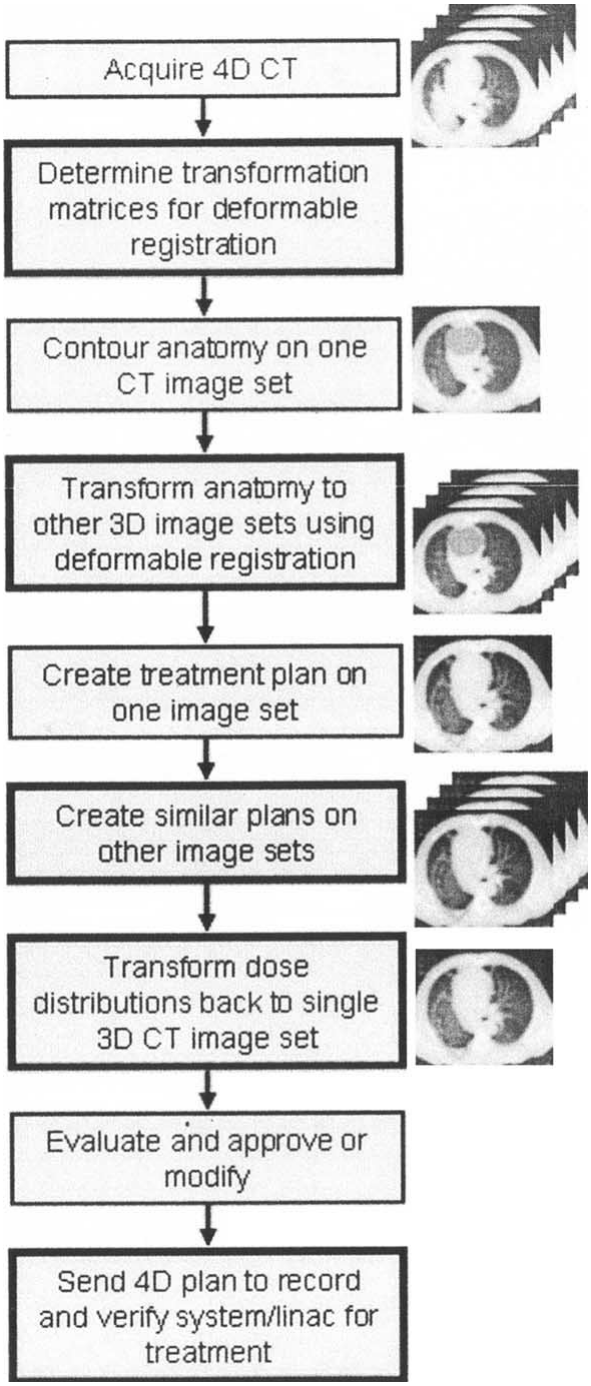

Figure 2.10: A flow chart of the 4D-planning process. [33]

2.3.3 4D treatment planning

Once the 4D CT scans have been acquired, the next problem is how to use the data for treatment planning. Because the amount of data is of the order of 10 times those for a standard CT image set, there is an order of magnitude increase in the amount of work required to obtain a 4D treatment plan. As, this increase in workload is so large, 4D planning requires automation. The tool that facilitates the automation of the 4D planning process is deformable image registration [34]. This technique allows the volumetric mapping of 3D CT image set in one respiratory phase to another phase. Once these transformations between breathing phases are known, processes such as anatomic contour definition, treatment planning and treatment evaluation on multiple data sets can be automated. With this automation, the workflow from a user interaction point of view is similar for 3D and 4D.

The anatomy (OAR) and tumor) drawn on the reference CT is mapped to the CT scans of the other phases using the deformable registration transformation matrices, which creates automatically contours. Deformable image registration is not an exact science and errors will be introduced in the process. A (crude) method of verifying the validity of the transformation is to visually correlate the automatically created contours with the CT anatomy itself.

Because 4D radiation delivery accounts for the change of tumor position with time, the concept of a 4D PTV naturally appears, called Internal Target Volume (ITV). The parallel appears between rescanning and replanning patient midway through the treatment course to account for interfraction motion, where clearly different PTV would be created for the subsequent plan change with time. This rationale can be applied to the case of intrafraction motion, where a distinct PTV associated with each respiratory phase is created as both the CT geometry and treatment plan change with time, although over a much shorter time period. Once the anatomy has been defined, the treatment beams are added.

2.3.4 Motion mitigation

There are many ideas of how to mitigate effects due to temporal changes in anatomy. Such changes can be taken into account during planning simply through the use of the ITV approach [35] or using the more sophisticated approach of 4D-inverse planning [36]. Alternatively, treatments planned on a static geometry can be delivered in a way that compensates for changes of the anatomy. This approach is followed in beam rescanning, gating, and tracking. For the three latter techniques, the common expectation is that none of the methods represents the ultimate solution. Rather, different approaches have different advantages in different scenarios. Many of the motion management strategies rely on motion information acquired prior to the actual treatment (for example, 4D CT). In this case, one should always be aware that 4D CTs only provide a snapshot of the present motion and the resulting uncertainties at the time of treatment should be taken into consideration. The parameters which should be considered in the choice of the motion management approach include the following:

- the facility specifications such as scanning speed (energy modulation speed, time for lateral position adjustment, and dose rate), the available scanning method (raster-scan, spot-scan, and continuous scan), the deliverable dose resolution, the time latency (in actively controlled beam delivery), and the available imaging tools;

- patient specific parameters such as the target volume and location, surrounding critical structures, motion parameters, clinical status, and patient compliance, and the fractionation scheme used.

Below, the current status of motion management approaches in particle therapy is summarized and areas for future investigation are identified.

Margin-based approach

The use of margins alone for motion management is likely not sufficient for scanned particle beams because of interplay effects [37]. Nonetheless, margins and ITVs could be required also for scanned particle beam treatments since some motion management techniques are of limited precision and thus margins have to cover for the uncertainties. This is especially important for rescanning which does not perform any surveillance of the patient's motion and thus relies on margins. Implementation of the ITV, or any margin approach, using concepts defined for photon beams may well be invalid for protons and heavy ions due to the high sensitivity of the dose distribution to density variations in the entrance channel.

Rescanning

With rescanning [38], the ITV/PTV is irradiated multiple times within each field delivery, with the rationale that interplay effects will be smoothed out and thus a homogeneous coverage of the CTV is achieved. However, this will inevitably be at the cost of the therapeutic dose in the internal margins that form the PTV. Multiple delivery modes for performing rescanning exist, with the most prominent distinction being whether the scans are first repeated within a 2D energy layer (slice-by-slice rescanning) or the whole 3D volume is rescanned (volumetric rescanning). In both modes, different repainting strategies can be employed as, for example, scaled rescanning, for which the beam weight of each scan position is divided by the number of rescans or isolayered rescanning, for which fixed beam weights are applied per rescan. When implementing rescanning, particular awareness has to be given to machine specifications such as the scanning speed, the scanning method, and the dose deliverable resolution which can place limitations on the rescanning approach.

For the determination of the appropriate repainting strategy, the fractionation scheme, number of fields, as well as the number and temporal sequence of the energy layers con-

tributing to a beam position should be considered. For a single-field-uniform-dose plan, all of these parameters have been shown to contribute an intrinsic rescanning effect, which should be considered in the decision of how many rescans and what type of rescanning should be employed. Extensive simulations and experimental work are required to comprehensively evaluate these effects for different patients and plan parameters. Synchronization effects due to the periodicity of target motion and individual rescans, especially for repetitive scaled rescanning, are a potential source of large underdosage in the CTV [39]. Their impact has to be studied more extensively and possible solutions, such as the introduction of random pauses between rescans, have to be investigated.

Gating

Gating refers to an irradiation technique in which the beam is turned on during specific motion phases only, the so called gating window [40]. Gating thus requires a motion monitoring system that determines the motion phase of the patient during treatment delivery. A review on motion monitoring methods was given by Murphy [41]. Gating has been used for treatment with scattered particle beams for several years. For application to scanned beams, the residual motion within the gating window and the scanning process interfere, leading to a residual interplay effect. To mitigate this interplay effect, a combination of rescanning and an increased overlap between neighboring pencil beams have been proposed.

With respect to treatment planning, gating requires optimization of gating window size and the parameters that mitigate the dosimetric effect of the residual interplay. Robustness analysis to investigate the effect of baseline drifts, limited precision of the motion monitoring system, and change in patient breathing parameters are also required.

Part II

Experimental Work

Chapter 3

Analytical results

The CPT at PSI recently started treating moving tumors, using pencil beam scanning in the regime of volumetric rescanning. Rather than delivering dose per fraction at once, the dose of each spot is divided into smaller parts. Pencil beams scan through a target volume multiple times until the original fraction dose is accumulated. SFUD fields are currently used at CPT PSI for 4D treatments. In the scope of this project, properties of rescanned delivery have been tested for SFUD and for patched fields.

In the course of this chapter what has been done will be explained and the analytical results obtained will be reported and discussed.

3.1 Patch field

In the delivery of proton therapy, it is sometimes necessary to split a field into two or more parts, since the dimensions of the target volume exceed the deliverable size of the gantry. In Gantry 2 the maximum area that can be treated is of 12 cm in T direction and 20 cm in the U direction, but the size of patches can be reduced on a software level, modifying the steering files setup. Conventionally the setup is set to 11 cm for the T direction and 19 in the U direction, to keep 5 mm of margin between the target and the

maximum lateral margin reachable by the beam.

The use of multiple-field patching can assist in maintaining target coverage and conformity [23] [44]. This technique has been created initially to combine two independent fields to treat a single target volume, to avoid critical structures near the target [45].

Typical proton patched-field treatment split one field in two, where one treats a portion of the target and the second field treats the remainder of the target; generally the two portions correspond to the half of the total volume. The challenge of using this technique is to achieve a homogeneous dose distribution also in the patching zone, since the presence of hot and cold spots in the target may lead to suboptimal treatment. In 4D-plans this goal is made more difficult due to the presence of the movement of the target and of the OARs.

The target dose uniformity may be improved in spot-scanning treatments by optimizing dose spot weights in the area where the dose distributions overlap or get in contact [46]. Alternatively, spot sizes may be chosen such that the penumbrae from various beam spots contributing to the patch region are selected to sum to a homogeneous dose [47]. These techniques are possible due to the flexibility of spot-scanning deliveries and require the ability to choose a wide range of spot intensities, sizes, and locations within a target.

For this study, different configurations were investigated, in order to find the best one. Two parameters were changed: number of volumetric rescanning (1,4 or 8 rescans) and overlapping region between the patches (0, 1 or 2 cm overlapping), so that we had 9 different combinations for every plan. No greater overlap has been investigated, to avoid the risk of obtaining more patches, while a greater number of rescans would lead to a release time too high. 4DDC in case of rescans and/or patch overlap proceeds with an optimization of dose spot weights, in order to split the total dose of the spot, until a minimum is reached. Under this lower limit the number of rescans will be limited. Currently, 4D-treatments that require patches are rejected or are treated with normal

3D-plans.

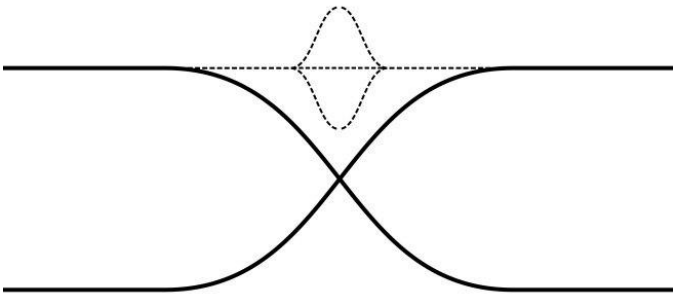

Figure 3.1: Schematic representation of an overlapping patch field with desired homogeneous dose and possible hot and cold spot.

3.2 4D Dose Calculation

Treatment Planning Systems (TPS) that calculate treatment plans are complex software systems, which makes comprehensive testing, commissioning and quality assurance difficult. In addition to this, the delivery of a PBS treatment plan requires at least two transformations of the resultant 3D Bragg peak fluence map resulting from TPS optimization [49]. In a first step, this needs to be converted into machine-readable files, which in a second moment have to be correctly interpreted and delivered by the treatment machine. Both transformations are potential sources of errors which can be hard to detect, especially given the complexity of individual fields. Indeed, from the machine point of view, the translation of the fluence map from TPS to treatment machine is not always straightforward. Due to dynamic effects, as well as random "noise" during delivery (e.g. magnet hysteresis, current fluctuations), the actually delivered spot positions can vary from the planned positions by the order of up to a millimeter. For instance, at the PSI Gantry 2, the relative and absolute spatial accuracy of each pencil beam need

to be substantially improved through the use of spot specific positional offsets obtained from an initial delivery of each field in an approach called "teaching" [48].

4DDC requires motion vectors and plan files: the former are extracted by a 4DCT or a 4DCT(MRI) while the latter are generated starting by plan information and are created during the 4D workflow (shown in Figure 3.2). Plan files are of two kinds: TPS field and plan data, and steering files.

TPS field and plan data

A typical PBS plan is made up of one or several fields, where each field consists of several thousand pencil beams delivered at a given gantry and a table angle. During the planning step, for each of these angles, Bragg peaks are placed on a rectilinear grid inside the target (with a user-defined margin) and iteratively optimized to achieve a homogeneous dose distribution in the target [23] [24]. If the fields are optimized one by one, this results in an SFUD plan. If the individual fields are allowed to be non-homogeneous, better OAR sparing can be achieved as part of an IMPT plan. As a result of this optimization, each such field in the treatment planning system is represented as a set of binary files with a standard header and a data block containing, for each pencil beam, its energy, lateral position and the optimized number of protons.

Steering files

For the machine to deliver a planned field, the spot by spot information need to be translated into machine parameters which are fed to the treatment machine by steering (machine control) files. This step is handled by a separate program, the so-called Steering Files Generator (SFGen). Relevant data in these files for the 4DDC are the beam line settings required to provide the desired energy, the currents in the sweeper magnets for the required lateral deflection and the position of the patient couch (expecially in case of large targets that require field patching), as well as the extraction of the telescopic

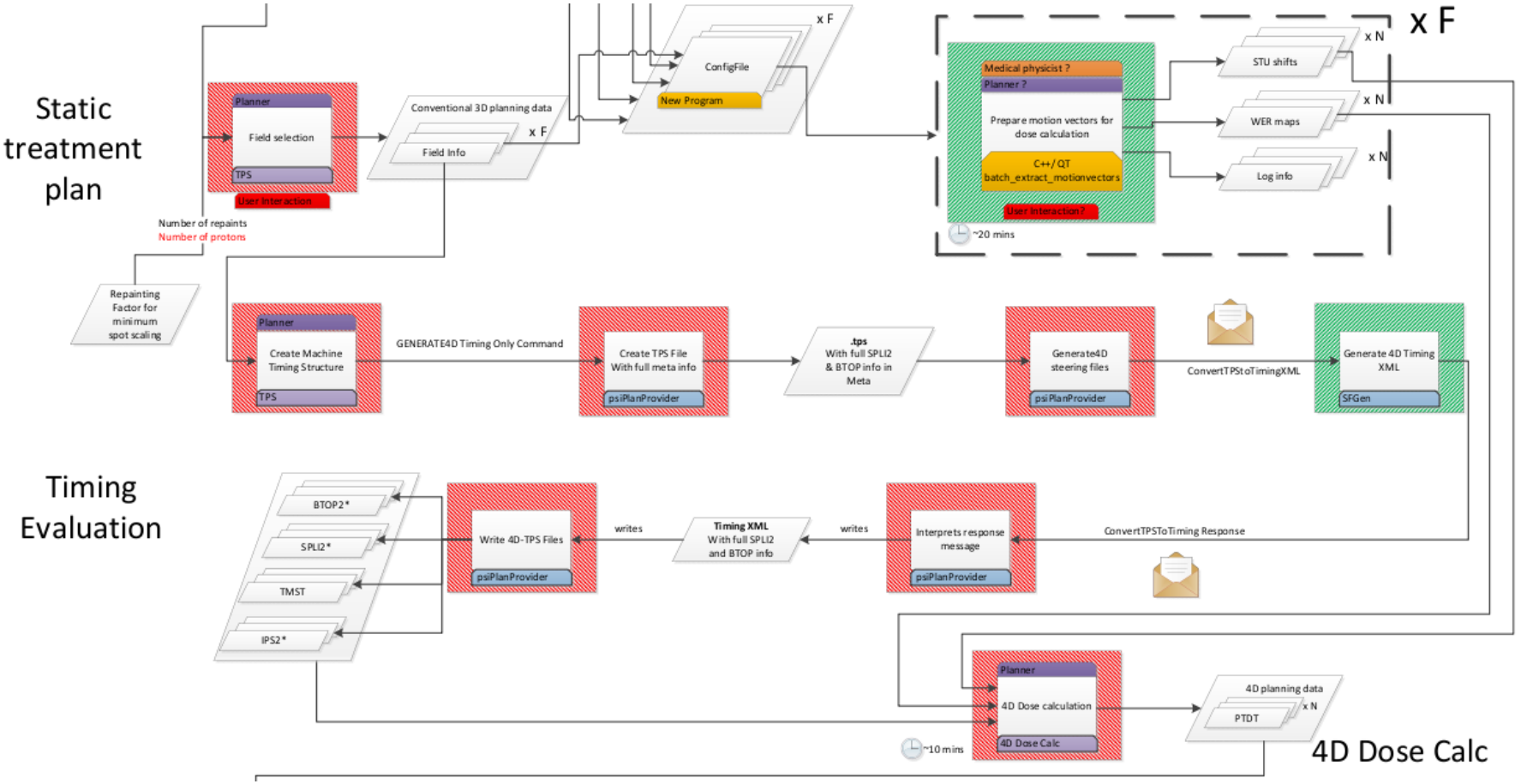

Figure 3.2: Schematic representation of the last part of 4D workflow.

nozzle (a feature of Gantry 2 [12]), which impacts on the beam profile in air.

The steering files are binary files that contain control sequences for beam line settings, table motions, nozzle positions (extraction) and spot deliveries. In addition, Gantry 2 is equipped with an automatic, single thickness pre-absorber plate (water equivalent thickness of 4.1 cm) which can be introduced to reduce proton energy sufficiently enough to deliver Bragg peaks to the surface of the patient. The necessity of this plate for any spot is also sequenced into the steering files. For each spot, the required currents for both sweeper magnets as well as the required number of monitor units in the primary beam monitor are defined. This "forward translation" from positions to magnet currents is performed by SFGen using a 2D higher order polynomial fit. For the steering file based dose calculation, the expected spot positions are then reconstructed from these nominal currents of the sweeper magnets. However, as an analytical inversion of this fit is difficult, this reconstruction is performed using an independent fit.

Finally, the monitor units (MU) for each pencil beam can be calculated directly form the number of protons N_p according to [49]

$$MU \;=\; G_{el} \cdot G_{IC} \cdot \frac{1}{\rho}\frac{dE}{dx}(E) \cdot C(E) \cdot e \cdot N_p \tag{3.1}$$

where $\frac{1}{\rho}\frac{dE}{dx}$ is the stopping power and e the elementary charge. G_{el} is the gain of measurement electronics [MU/nC], determined by characterization measurements. G_{IC} is the ion chamber gain [g/MeV/cm^2], depending on the geometry of the detector and obtained by Faraday cup measurements [50]. C(E) is an energy dependent factor that was introduced to correct for energy dependent deviations observed in the Faraday cup measurements of the ion chamber gain. These Faraday cup measurements have traditionally been the basis for absolute dosimetry at PSI, thus the monitor chambers are calibrated in number of protons and dose to water. While this is a somewhat uncommon approach, it allows to break the dose calculation to the single proton level.

Calculation

The TPS for dose calculation developed at PSi is based on ray casting pencil beam model [52], all information is taken from the files described above. First, a dose grid in the beam coordinate system (s, t, u where s is parallel to the incident beam direction) is created covering a volume of interest in the patient geometry. The spacing of the dose grid point can be arbitrary and does not depend on the resolution of the underlying CT image. The TPS then calculates successively the dose for each proton beam at all affected dose grid.

The overall dose at one grid point position is given by the sum of doses from all contributing pencil beams. To create a continuous dose distribution in the patient (CT) coordinate system, the dose in between the dose grid points is then interpolated. Typically, the dose grid size for calculations in the s,t,u coordinate system is 5 x 5 x 5 mm.

To extend this to a 4D dose calculation, the pencil beam model has been adapted to cope with target motion by adding time-dependent displacements for motion in the t and u direction, respectively [51]. The starting point for the 4D dose calculations is a static 3D treatment plan of TPS represented by a set of proton pencil beams (the spot list) describing the position and the characteristics of each applied pencil beam. In addition, for the 4D calculation individual time stamp (TS) is calculated for each pencil beam. The TS depends on the number of protons delivered at each position and a set of hardware parameters. The TS changes, for example, depending on the scanning path and velocity (required dead times to adjust the beam position) and, if applied, the kind of rescanning (2D/3D, scaled/iso-layered, number of rescans). This combination of a pencil beam specific spot list and a set of timestamps completely describe the temporal characteristics of treatment field delivery.

As for the motion of the patient geometry, this can be taken into account by using pre-calculated displacement-maps derived for each motion phase (MP). The dose calculation

is then performed on a continuously moving geometry, employing a linear interpolation for the motion between any two MP. Thus the displacements are continuously calculated and take into account in the dose calculation for a given pencil beam TS.

Finally, in order to deal with time-varying changes in densities and therefore proton ranges, the algorithm uses pre-calculated density-variation-maps once again for each MP. Water equivalent ranges at TS in-between two MP are chosen form the density-variation-map closest time.

3.3 Clinical cases

For this study, 3 different patients were analyzed, with motion extracted by their 4D CT, like for normal treatment planning. For the patient 16254 a treatment plan was also studied with an extrapolated motion by a 4DCT(MRI) [53]. We took the decision of simulating a motion, extracted by a volunteer's 4DMRI, for three motivations: analyze the behavior of a plan with 4 patches with more motion, add an intermediate configuration between 4 mm of motion and 20 mm, confirm some indications that emerged from others results. The usage of motion extracted by a 4DMRI gives the benefit of a more realistic simulation of the respiratory motion. 4DCT motion is extracted and supposed periodical combining 8 phases of the respiration (more than 8 CTs risk to give a too high dose to the patient), while with MRI it's possible to scan the motion for some minutes.

The limited number of clinical cases analyzed is due to a lack of patients treated, since oncologists, generally, prefer to treat mobile tumors with other techniques.

Later the clinical cases will be exposed, reporting: kind of tumor, the extension of the motion, an overview on the number of fields and number of patches, if preabsorber was needed, and the size of the tumor in beam's eye view. A representation of the CTV, PTV and the patch zone will be included for all cases.

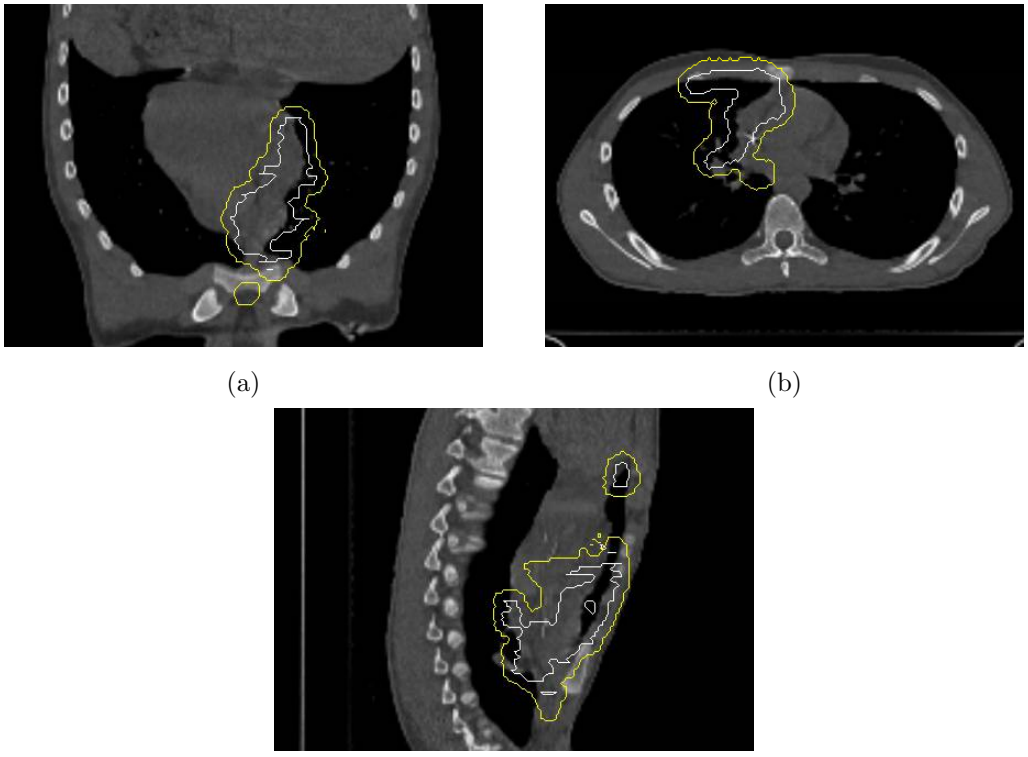

(a) (b)

(c)

Figure 3.3: Representation of the CTV (white) and PTV (yellow) for the patient 16254. Patch zone is shown with a with line. a coronal view, b axial view, and c sagittal.

Patient 16254

- Non-Hodgkin lymphoma
- Small motion ($\sim$ 2 mm)
- 2 fields, 1 with 2 patches, 1 with 4 patches
- Preabsorber insert
- Dimension: 22.8 cm in U direction, 12.4 cm in T direction

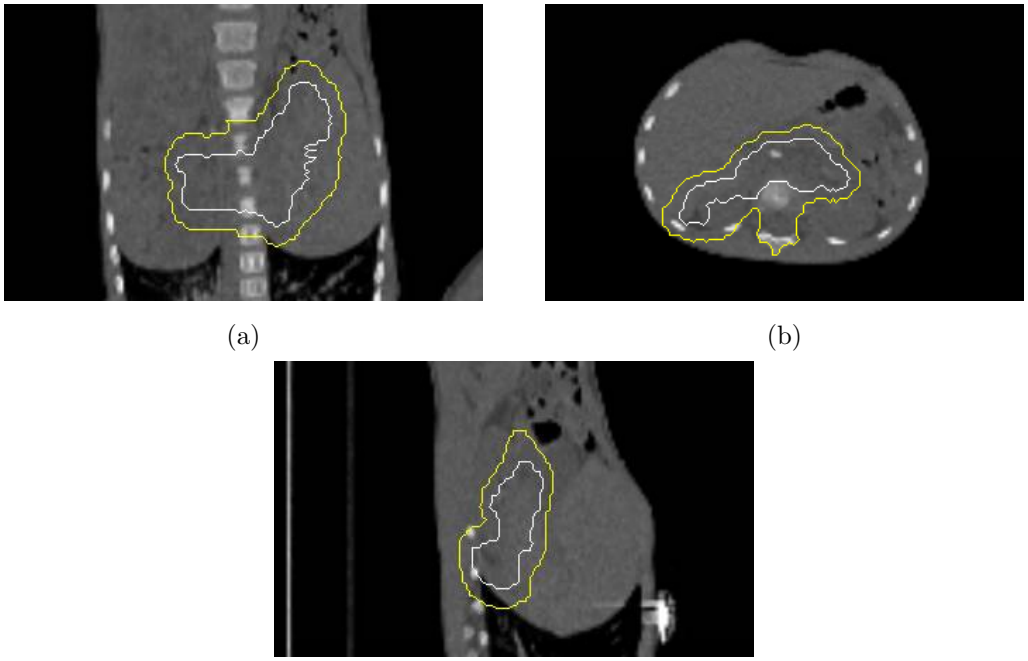

(a) (b)

(c)

Figure 3.4: Representation of the CTV (white) and PTV (yellow) for the patient 17914. Patch zone is shown with a with line. a coronal view, b axial view, and c sagittal.

Patient 17914

- Neuroblastoma III
- Moderate motion ($\sim$ 4 mm)
- 3 fields, 1 not patched, 2 with 2 patches
- Preabsorber mixed
- Dimension: 11.6 cm in U direction, 12.8 cm in T direction

Patient 16254 MRI

- Non-Hodgkin lymphoma

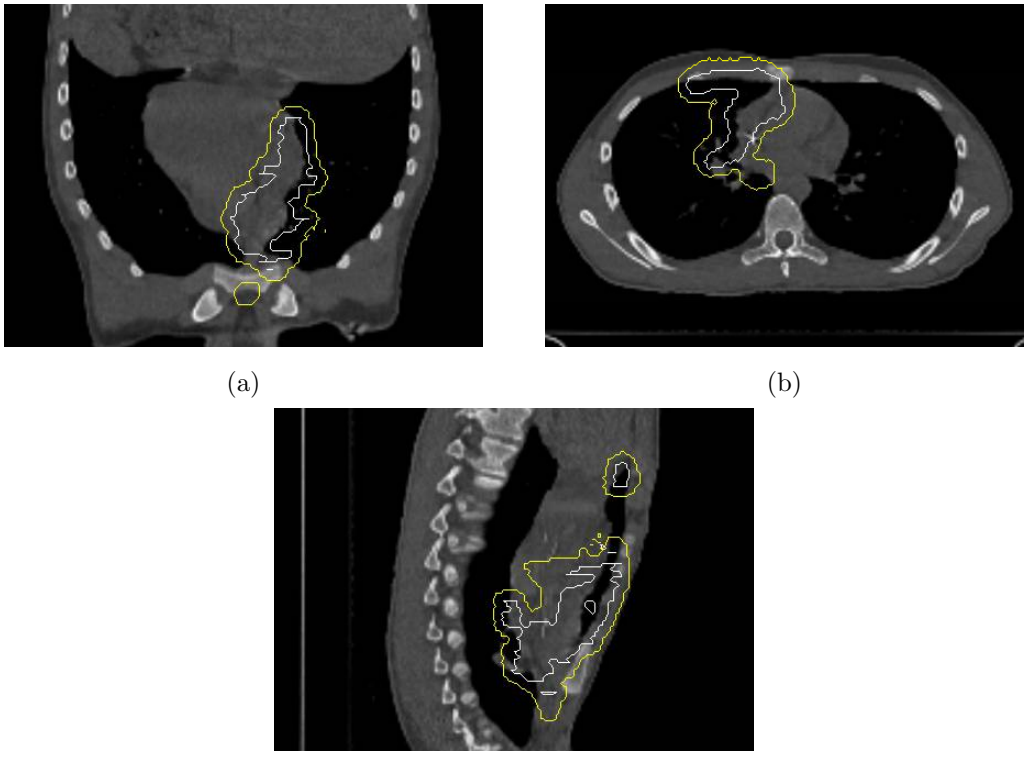

(a) (b)

(c)

Figure 3.5: Representation of the CTV (white) and PTV (yellow) for the patient 16254 MRI. Patch zone is shown with a with line. a coronal view, b axial view, and c sagittal.

- Moderate motion ($\sim$ 10 mm)
- 2 fields, 1 with 2 patches, 1 with 4 patches
- Preabsorber insert
- Dimension: 22.8 cm in U direction, 12.4 cm in T direction

Patient 17522

- Retroperitoneal liposarcoma
- Large motion ($\sim$ 20 mm)

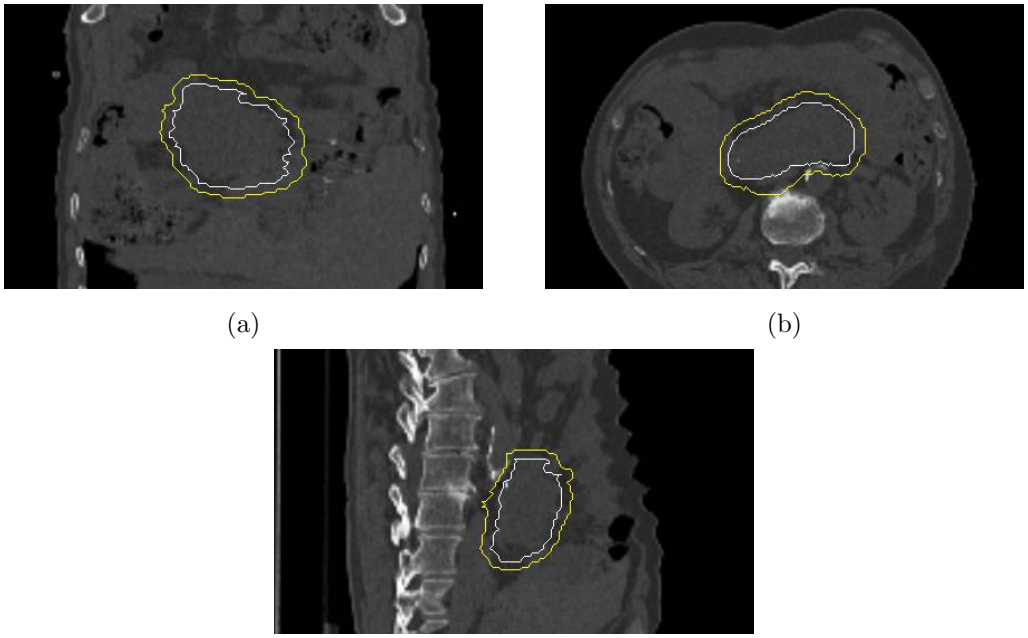

(a) (b)

(c)

Figure 3.6: Representation of the CTV (white) and PTV (yellow) for the patient 17522. Patch zone is shown with a with line. a is coronal view, b is axial view, and c is sagittal.

- 2 fields, 1 not patched and 1 with 2 patches
- Preabsorber out
- Dimension: 10 cm in U direction, 12.4 cm in T direction

3.4 Results

For all patients, we investigated 9 possible combinations of the 4D plan, 3 different setups of volumetric rescanning (1, 4, and 8) and 3 different overlapping setups (0, 1, and 2 cm), and 1 3D plan, assumed as the optimum plan achievable for the patient. The 4D workflow had to be hacked and modified since it was not possible to change the overlapping region.

After careful study, we have understood how to modify the procedure to generate the 4DDC, with a stand-alone version of SFGen. In normal procedure all the following steps were made in just one "click", but the timing.xml files should be changed:

- generation of field info files;
- generation by psiPlanProvider of a .tps file;
- creation of a timing.xml file (file that contain all the information about the 4D setup designed);
- insert the timing.xml file in psiPlanProvider to produce the files used by the optimizer to generate the dose calculation, the so-called plan files (IPS2, TMST, BTOP2, SPLI2, these files contain all information about spot position, energy and time of delivery).

We had to code a new stand-alone version of the TPS (wrote in Java) that does not proceed to generate by itself a timing.xml file, but that takes it from a folder where it was previosly stored. The timing.xml file has to be generated with stand-alone version of SFGen, in order to change manually the configurations of the setup that are desired. The procedure to create a 4D plan can take from 4 to 6 hours for each one.

All the results in the following tables and histograms were extracted with the software GUI Plan View. Histograms are the so-called Dose Volume Histogram (DVH), that are instruments that permit to visualize in a precise way the dose absorbed by a certain quantity of the volume, it is one of the most useful instruments to evaluate a plan. In tables are reported values of dose homogeneity measures as: D5-D95 and V95. These provide as results: the difference between the percentage of volume that receives 5% of the prescribed dose and the percentage of volume that receive 95% of the prescribed dose, and the percentage of volume that receive at least 95% of the prescribed dose. For D5-D95 a lower number corresponds to better results (since it means that the dose distribution

is steep and close to the optimum), while for V95 a higher number corresponds to better results (since it means that the volume of interest is all covered with enough dose).

3.4.1 Patient 16254

CTV

8 rescan		98.6	98.6	98.6
4 rescan		98.4	98.1	98.3
1 rescan	98.5	98.3	98	97.5
	3D	0 cm	1 cm	2 cm

Table 3.1: V95 [%] 16254 Plan CTV

8 rescan		8.3	8.7	8.4
4 rescan		9.2	9.6	8.9
1 rescan	8.4	9.7	10	9.9
	3D	0 cm	1 cm	2 cm

Table 3.2: D5-D95 [%] 16254 Plan CTV

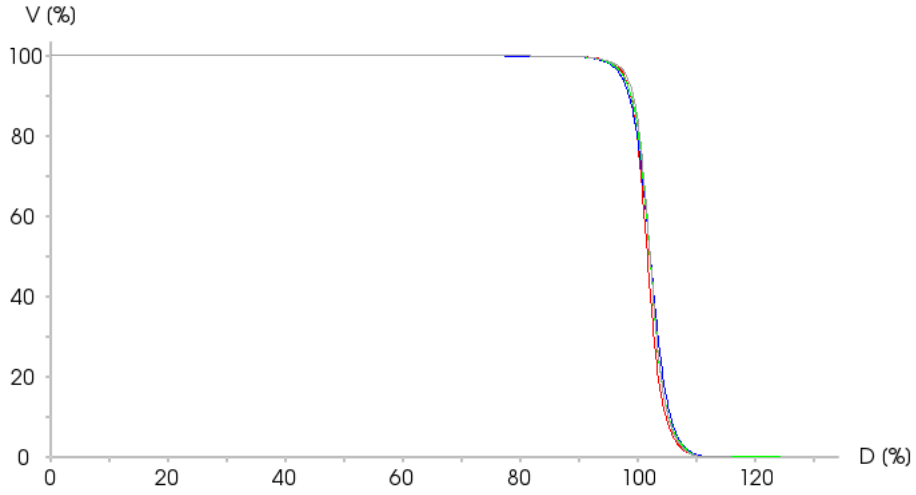

Figure 3.7: DVH for 16254 CTV. In red is represented 3D plan, in blue the best curve of 4D-1rescan, in green the best curve of 4D-4rescan, and in grey the best curve of 4D-8rescan.

PTV

8 rescan		92.3	92.2	91.8
4 rescan		91.7	91.7	91.3
1 rescan	92.3	91.5	91	90.4
	3D	0 cm	1 cm	2 cm

Table 3.3: V95 [%] 16254 Plan PTV

8 rescan		12.8	13.2	12.8
4 rescan		13.4	13.6	13.5
1 rescan	12.4	14	14.1	14.4
	3D	0 cm	1 cm	2 cm

Table 3.4: D5-D95 [%] 16254 PTV

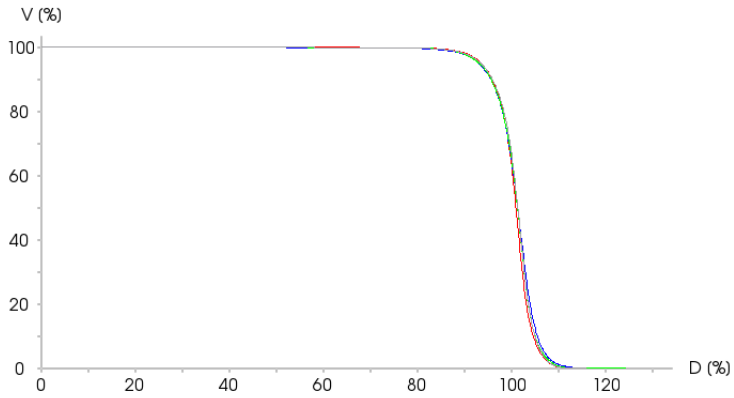

Figure 3.8: DVH for 16254 PTV. In red is represented 3D plan, in blue the best curve of 4D-1rescan, in green the best curve of 4D-4rescan, and in grey the best curve of 4D-8rescan.

3.4.2 Patient 17914

CTV

8 rescan		99.9	99.9	99.9
4 rescan		97.9	98.9	99.2
1 rescan	99.9	97.9	96.9	98
	3D	0 cm	1 cm	2 cm

Table 3.5: V95 [%] 17914 CTV

8 rescan		3.1	3.7	3.5
4 rescan		7.2	5.8	5.4
1 rescan	1.8	7.9	9.5	9
	3D	0 cm	1 cm	2 cm

Table 3.6: D5-D95 [%] 17914 Plan CTV

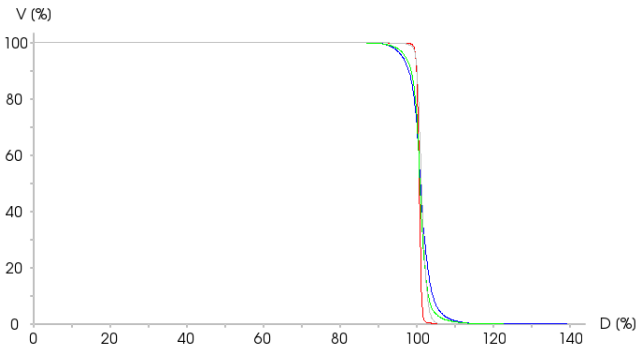

Figure 3.9: DVH for 17914 CTV. In red is represented 3D plan, in blue the best curve of 4D-1rescan, in green the best curve of 4D-4rescan, and in grey the best curve of 4D-8rescan.

PTV

8 rescan		95.1	94.9	94.8
4 rescan		91.2	93.6	94.1
1 rescan	92.3	90.8	90.9	91.5
	3D	0 cm	1 cm	2 cm

Table 3.7: V95 [%] 17914 Plan PTV

8 rescan		8.1	8.7	8.7
4 rescan		11.7	9.9	9.6
1 rescan	7	12.9	14.4	13.9
	3D	0 cm	1 cm	2 cm

Table 3.8: D5-D95 [%] 17914 Plan PTV

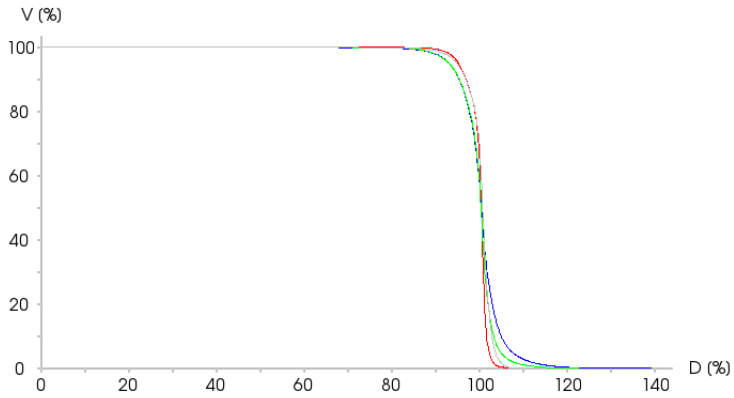

Figure 3.10: DVH for 17914 CTV. In red is represented 3D plan, in blue the best curve of 4D-1rescan, in green the best curve of 4D-4rescan, and in grey the best curve of 4D-8rescan.

3.4.3 Patient 16254 MRI

CTV

8 rescan		96.7	96.5	96.5
4 rescan		96.8	96.1	95.2
1 rescan	98.5	93	92	92.9
	3D	0 cm	1 cm	2 cm

Table 3.9: V95 [%] 16254MRI Plan CTV

8 rescan		10.1	9.8	9.6
4 rescan		11.1	12.1	13.7
1 rescan	8.4	15.6	16.4	15.5
	3D	0 cm	1 cm	2 cm

Table 3.10: D5-D95 [%] 16254MRI Plan CTV

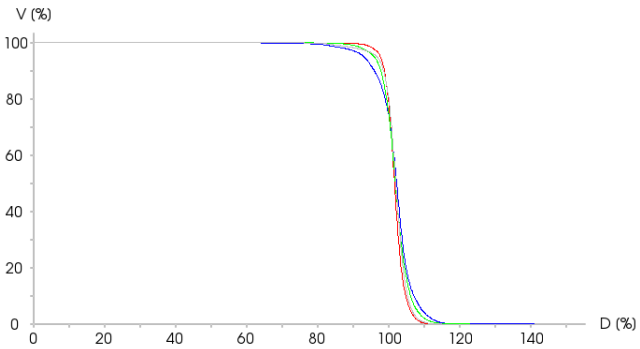

Figure 3.11: DVH for 16254MRI CTV. In red is represented 3D plan, in blue the best curve of 4D-1rescan, in green the best curve of 4D-4rescan, and in grey the best curve of 4D-8rescan.

PTV

8 rescan		89.4	89.2	90.2
4 rescan		89.8	88.2	88.4
1 rescan	92.3	87.7	85.7	87
	3D	0 cm	1 cm	2 cm

Table 3.11: V95 [%] 16254MRI Plan PTV

8 rescan		16.1	15.1	14.7
4 rescan		15.8	17.3	18.2
1 rescan	12.4	18.3	19.6	18.4
	3D	0 cm	1 cm	2 cm

Table 3.12: D5-D95 [%] 16254 MRI Plan PTV

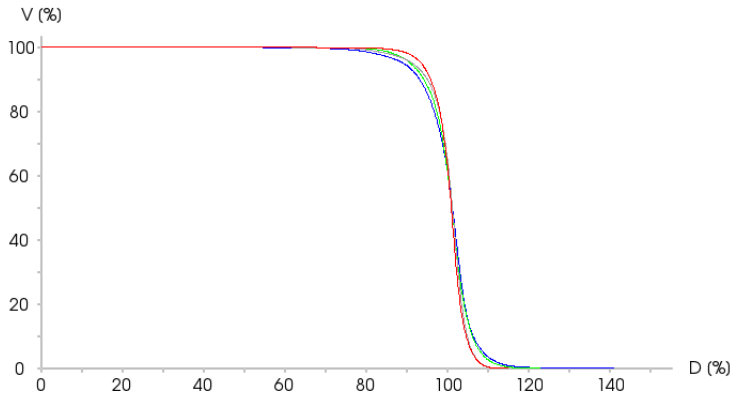

Figure 3.12: DVH for 16254MRI PTV. In red is represented 3D plan, in blue the best curve of 4D-1rescan, in green the best curve of 4D-4rescan, and in grey the best curve of 4D-8rescan.

3.4.4 Patient 17522

CTV

8 rescan		80.3	79.8	79.1
4 rescan		82.1	81.8	82.8
1 rescan	70.9	79.9	79.4	78.8
	3D	0 cm	1 cm	2 cm

Table 3.13: V95 [%] 17522 Plan CTV

8 rescan		27.3	25.4	23.6
4 rescan		25.4	26.5	25.9
1 rescan	23	31.4	32.4	32.8
	3D	0 cm	1 cm	2 cm

Table 3.14: D5-D95 [%] 17522 Plan CTV

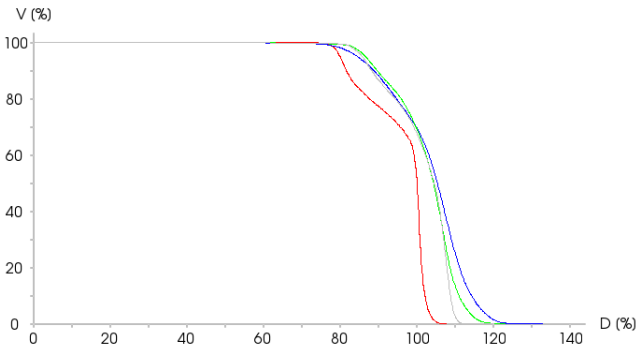

Figure 3.13: DVH for 17522 CTV. In red is represented 3D plan, in blue the best curve of 4D-1rescan, in green the best curve of 4D-4rescan, and in grey the best curve of 4D-8rescan.

PTV

8 rescan		68.7	67.2	66.6
4 rescan		69	69.1	69.2
1 rescan	60.1	67.4	67	66.4
	3D	0 cm	1 cm	2 cm

Table 3.15: V95 [%] 17522 Plan PTV

8 rescan		33.9	32.1	29.6
4 rescan		32	33.4	32.5
1 rescan	23.4	41.1	40.5	40.5
	3D	0 cm	1 cm	2 cm

Table 3.16: D5-D95 [%] 17522 Plan PTV

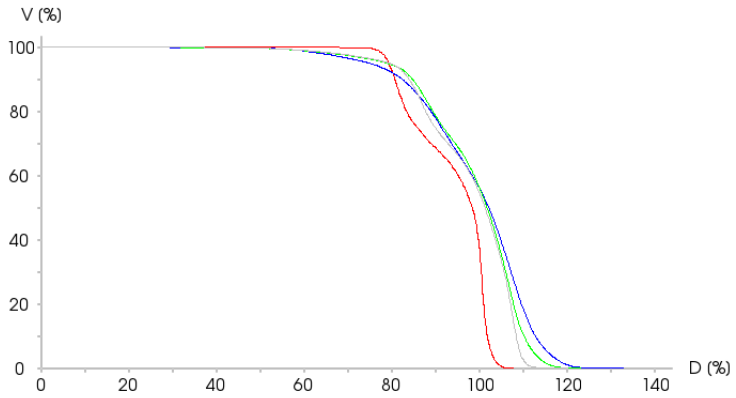

Figure 3.14: DVH for 17522 PTV. In red is represented 3D plan, in blue the best curve of 4D-1rescan, in green the best curve of 4D-4rescan, and in grey the best curve of 4D-8rescan.

3.5 Discussion of the results

Since the purpose of the study was to verify the possibility to deliver a 4D plan that requires patches, the first verification made was in a visual way. No tools existed to display the location of the patch, so during the thesis a workflow to permit the visualization of a single patch was elaborated. Starting by the steering files it has been generated a "Phys file", that is a human-readable kind of file containing a spot list with energies of protons and the location of the spot with reference to the isocenter of the patch. Once the list has been modified, in order to have only those spots pertinent to a given patch the dose is calculated again with an external tool called IDC [49]. Some example of dose for a single patch is shown in Figure 3.15. By a first coarse analysis, just visualizing the dose in the patching zone, no evidence of dose heterogeneity emerged.

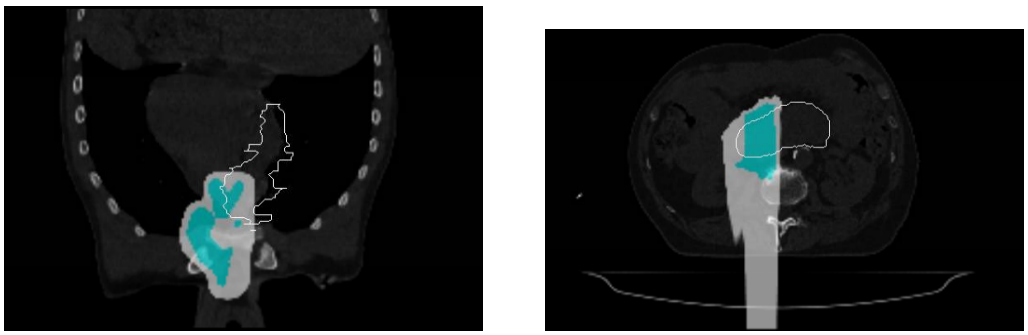

(a) (b)

Figure 3.15: In figure a it is possible to see the dose for just 1 patch of 4 for the patient 16254. In figure b it is possible to see the dose for just 1 patch of 2 for the patient 17522. In both pictures the contour of the CTV is also shown.

More significant studies were performed using dose homogeneity measures as: D5-D95 and V95.

All the results are shown in the subsection above, that is named "Results", and analysis on CTV results showed that size of overlap does not appear to influence the outcome in a systematic fashion, while an higher number of rescanning generally gives

better results. We found that the results could be split in 3 groups depending on their motion: small motion (under 2 mm), moderate motion (between 3 mm and 10 mm), strong motion (over 10 mm).

Patients are sorted for size of the motion, that is $\sim$ 2 mm for patient 16254, $\sim$ 4 mm for patient 17914, $\sim$ 10 mm for the patient 16254MRI, and $\sim$ 20 mm for the patient 17522 (this is also the maximum level of motion that is acceptable at PSI). We can see by values in Table 3.1 and in Table 3.2, that for small motion no mitigation is needed, as we reach acceptable coverage and heterogeneity level also with 1 rescan. We can see from Table 3.5, Table 3.6, Table 3.9, and Table 3.10 that with moderate motion, some mitigation start to be needed, since it is not reached an acceptable level of dose homogeneity or the increase in benefits is evident.

Analysis on the patient 17522 was tricky, since the plan needed was not a simple SFUD, but an IMPT, because the CTV was overlapping with an OAR (bowel) as shown in Figure 3.16. IMPT plans for 4D case are still not tested and not implemented in the clinical procedure. For those reasons all the results are not acceptable, but it is still possible to extract some useful information. From Table 3.13 and Table 3.14 it emerges that strong mitigation is needed and by a visual analysis of the shape of DVH (example in Figure 3.13) it is clear that increasing the number of rescanning and the overlapping region the algorithm of optimization tends to follow the shape obtained in 3D plan.

PTV analysis are less robust and not so significant, since the algorithm, that optimizes the dose, works on the optimization only of the CTV zone, and because the PTV concept is less meaningful in 4D treatments. However, some indications can be extracted, like that an increase of overlap generally gives better results, especially with mitigation of the motion involved.

In order to improve the general 4D workflow, we have designed a new version of the MATLAB script to select the correct mid-ventilation phase. The new version was created because patient 16254 was affected by local metastasis that, since they were

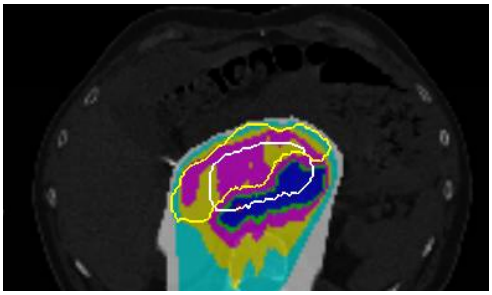

Figure 3.16: Dose distribution in 17522, it is possible to see that the overlapping between the CTV(white) and the bowel (yellow) corrupt the homogeneity of the dose. Blue indicates zone where the level is $\sim 100\%$.

located in a different region of the thoracic chest, could move in different ways. The version elaborated during this work permits to analyze the density of superficial spots of the tumor so as to cluster all the local metastases and return the mid-ventilation phase for each one. A more accurate analysis, and plan design can be done with the new script as we can perfectly know if all the metastases have the same mid ventilation or not. The cluster analysis works on information extracted from a DICOM file and the clustering algorithm is the so-called DBSCAN (Density-Based Spatial Clustering of Application with Noise), a nonsupervised algorithm of clustering. A nonsupervised cluster algorithm was chosen since no previous information about the number or location of the clusters are know a priori. The output of the program is a figure that shows the shape of the tumor with a different color for every metastasis and pictures that show the movement of the tumor and the midventilation phase.

Chapter 4

Experimental results

Following the analyzes described above, experimental checks were carried out, so as to examine the correct delivery of the beam. In the chapter the experimental setup will be presented, as well as the techniques used for the correct beam delivery and the results of the gamma analysis. A short discussion will follow to comment the results.

4.1 Experimental setup

All the acquisitions were done at Gantry 2 since, at the time of my thesis internship, it was the only gantry in which it was possible to make 4D treatments, now also Gantry 3 it's available. The plans were recalculated in water geometry and the specific depth was simulated with plexiglass, that has a "water equivalent thickness", for protons, of 1.7 [54]. A 2D array detector (PTW Octavius 1500) was mounted on QUASAR Respiratory Motion Platform, and the delivery was regulated by an in house gating system.

PTW Octavius 1500

The OCTAVIUS Detector 1500 is an ion chamber matrix in a plane used for radiation therapy verification and quality control. An ionization chamber, basically, consists of

a gas volume between two electrodes connected to a high voltage supply of typically 100V to 1000V. In this gas volume, ionizing radiation creates ion pairs. These, being positive and negative charge carriers, are attracted by the electrodes thus creating a current which can be measured by an electrometer. Gas (air) volumes vary for 0.005 cm^3 to 50000 cm^3, and the corresponding currents can be between 10^{-14} A and 10^{-7} A. Using non-polar fluids, liquid-filled ionization chambers can be realized. Utilizing ion chambers avoids radiations defects, the major drawback of solid-state detectors

The plane-parallel ion chambers are 4.4 mm x 4.4 mm x 3 mm in size (0.06 cm^3), and the center-to-center spacing is 7.1 mm. In total 1405 ion chambers are located in a chessboard matrix, providing a maximum field size of 27 cm x 27 cm. This device has a range of use that goes from 0.5 Gy/min to 48 Gy/min, with a resolution of 0.1 mGy and 0.1 Gy/min [55].

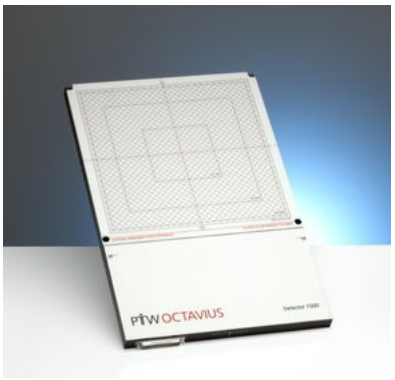

Figure 4.1: PTW OCTAVIUS 1500 [55]

Gating system

A gating system has been used as a trigger for the delivery, so that all irradiations start when the platform was in a certain position. This technique was introduced to reduce the delivery uncertainties derived by a random choice of the starting point. To check the motion it has been used an optical tracking system, Polaris SPECTRA, produced

by Northern Digital Inc. [57] .

Polaris SPECTRA is a position sensor that measures the location of either active or passive infrared markers. Three-dimensional localization relies on stereo photogrammetry theory to triangulate a marker point from multiple calibrated views of the scene that are acquired with two sensors embedded in the device. The Position Sensor emits infrared (IR) light from its illuminators, like the flash on a conventional camera. The IR light floods the surrounding area and reflects the Position Sensor off passive sphere markers (on passive tools) or triggers markers to activate and emit IR light (on active wireless tools). A System Control Unit (SCU) activate the markers on the active tools, causing them to emit IR light, the Position Sensor then measures the positions of the markers and calculates the transformations (position and orientation) of the tools to which the markers are attached. The Position Sensor transmits the transformation data, along with status information, to the host computer for collection, display, or further manipulation. When connected to the SCU, the Position Sensor can track three types of tools: passive tools, active wireless tools, and active tools.

Figure 4.2: The optical tracking system, Polaris SPECTRA [56]

Motion Platform

The motion was simulated using two different kinds of curves to simulate moderate and strong motion, the 2D array was mounted on QUASAR Respiratory Motion Platform.

The QUASAR Respiratory Motion Platform is designed to move an existing phantom

or detector with programmable respiratory and sinusoidal motion profiles for patient-specific QA. The platform, 35 x 35 cm, allows moving in the superior/inferior direction with amplitudes up to 2 cm.

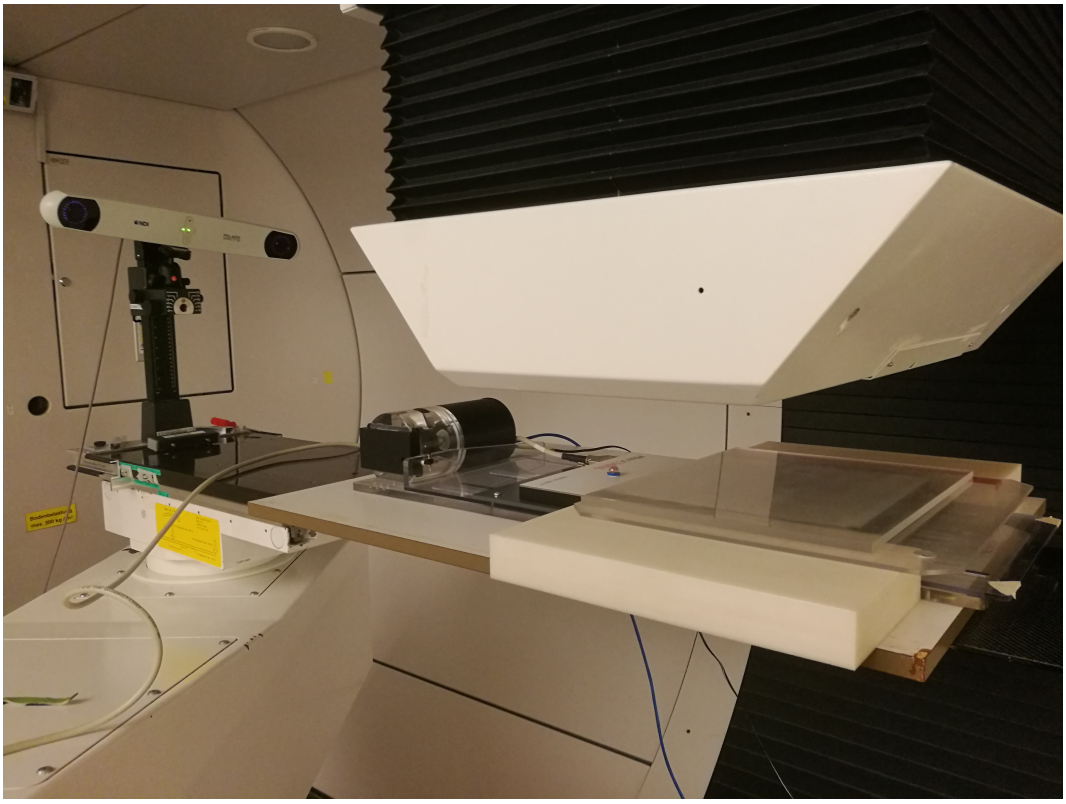

Figure 4.3: Representation of the full experimental setup used at Gantry 2.

Teaching

All fields were taught and boosted. To generate steering files from the TPS system, sweeper magnet currents are calculated from the nominal spot positions by a 2D higher order polynomial fit. However, as Gantry 2 was designed to allow for fast energy changes for 3D scanning, dynamic and magnetic hysteresis effects are not fully addressed by these static sweeper maps. To account for such effects, additional spot by spot offsets are determined based on positions measured in the nozzle [49]. This process, referred to as

steering file teaching, is performed as part of the plan verification. After the first delivery of an unmodified steering file to a phantom, the logged position errors (of the order of one millimeter) are used to calculate corrections, using a smoothing approach to avoid over-correcting random effects. After such corrections, the steering files are designated as being 'taught' [48].

4.2 Results

The results presented here were obtained with gamma analysis made with Verisoft software. The gamma score presented in tables offers a composite analysis with a percent dose diffence (DD) and a distance-to-agreement (DTA) collapsed into one parameter. The gamma is defined as the square root of a linear quadratic addition of the two factors, while they are provided in relative magnitude to their acceptance criteria (C_{DTA} and C_{DD}) as shown [59]

$$\Gamma = \sqrt{\left(\frac{DTA}{C_{DTA}}\right)^2 + \left(\frac{DD}{C_{DD}}\right)^2}.$$

The delivery of a plan is acceptable if it satisfies the minimum value of 90%.

There are presented also tables with time of delivering every field test, with the percentage indication of how much is the increase respectly to the deliver of a 3D/1 rescan plan.

4.2.1 Patient 17914

Table 4.1: Gamma analysis of patient 17914 Field 1

8 rescan	x	93.1	95.1	93
4 rescan	x	92.1	93.1	94.1
1 rescan	-	-	-	-
	3D	0 cm	1 cm	2 cm

Table 4.2: Time of delivering Field 1 of patient 17914

8 rescan	x	8'52" (521%)	8'49" (519%)	11' (1219%)
4 rescan	x	5'05" (299%)	5'04" (298%)	5'03" (297%)
1 rescan	1'42"	-	-	-
	3D	0 cm	1 cm	2 cm

Table 4.3: Gamma analysis of patient 17914 Field 2

8 rescan	x	86.3	-	89.9
4 rescan	x	88.4	-	87
1 rescan	-	-	-	-
	3D	0 cm	1 cm	2 cm

Table 4.4: Time of delivering Field 2 of patient 17914

8 rescan	x	10' (1071%)	-	11' (1219%)
4 rescan	x	5'11" (555%)	-	5'09" (552%)
1 rescan	56"	-	-	-
	3D	0 cm	1 cm	2 cm

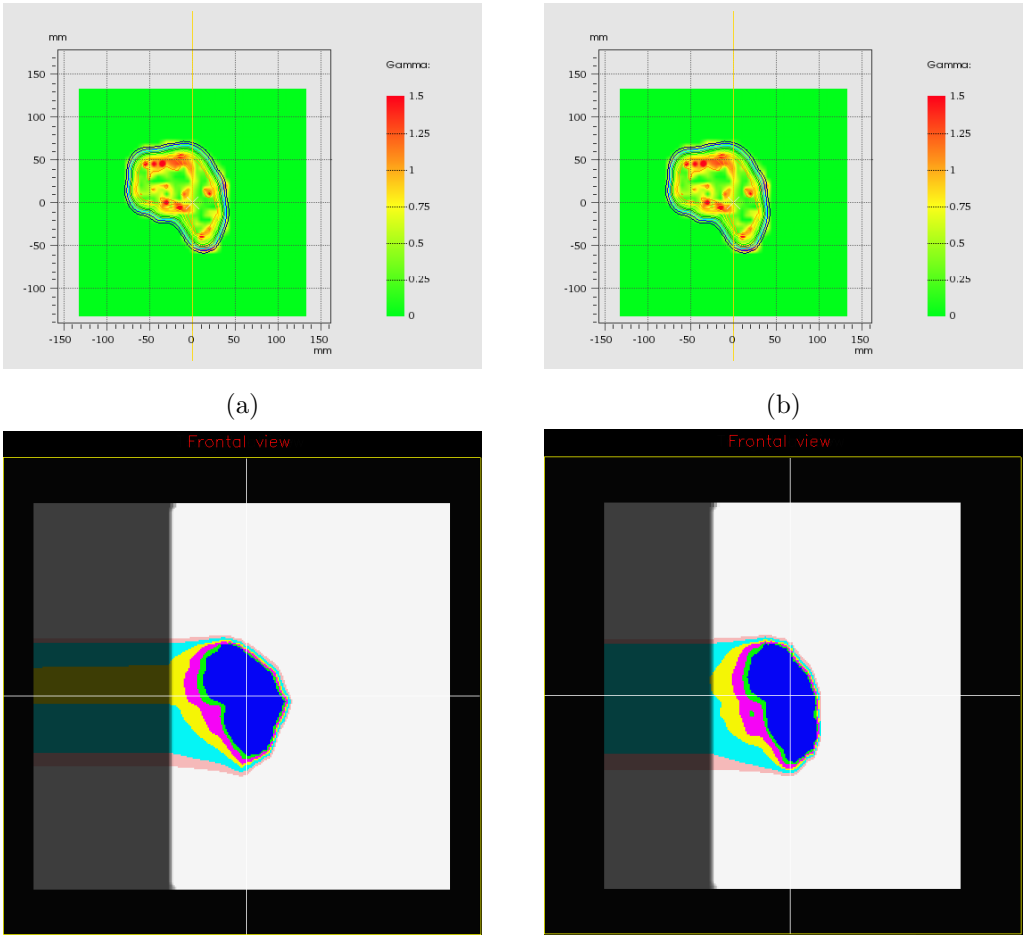

(a) (b)

(c) (d)

Figure 4.4: 17914 2 cm overlap 4 rescan, 6.8 water equivalent. On the left there is a representation of F1, while on the right there is a representation of F2.

4.2.2 Patient 16254

Table 4.5: Gamma analysis of patient 16254 Field 2

8 rescan	x	97.9	97.8	98.3
4 rescan	x	99	98.6	97.4
1 rescan	-	95.7	92.2	91.3
	3D	0 cm	1 cm	2 cm

Table 4.6: Time of delivering Field 2 of patient 16254

8 rescan	x	11'52" (520%)	12'04" (528%)	12'16" (537%)
4 rescan	x	7'12" (315%)	6'59" (306%)	7'05" (310%)
1 rescan	-	2'17"	2'44"	2'25"
	3D	0 cm	1 cm	2 cm

Table 4.7: Gamma analysis of patient 16254 Field 2 with strong motion

8 rescan	x	85.8	87.9	90.2
4 rescan	x	-	-	-
1 rescan	-	-	-	-
	3D	0 cm	1 cm	2 cm

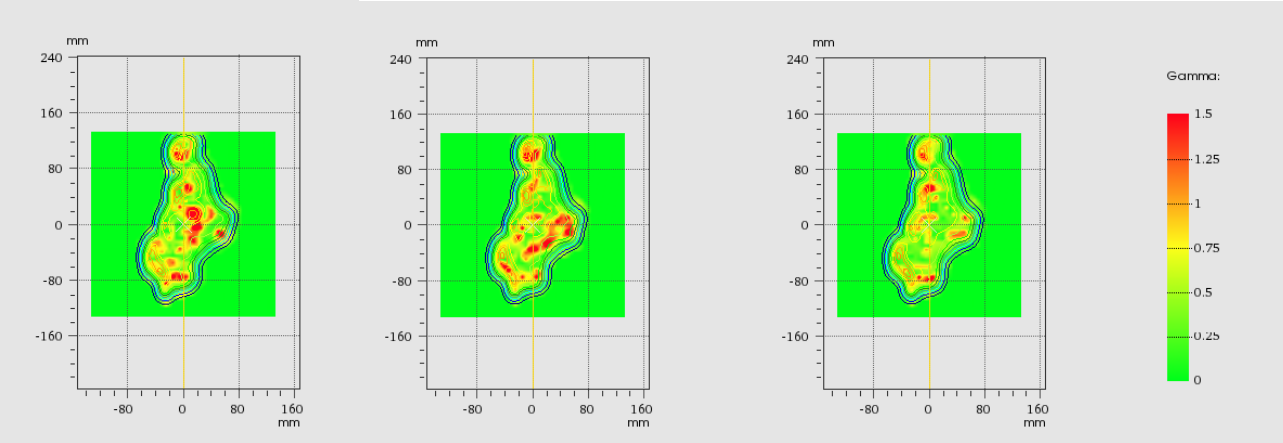

(a) (b) (c)

Figure 4.5: Comparison of gamma score for 16254 F2 delivered with strong motion simulation.

Table 4.8: Gamma analysis of patient 16254 Field 1

8 rescan	x	-	-	90.2
4 rescan	x	-	-	-
1 rescan	-	95.6	-	92.3
	3D	0 cm	1 cm	2 cm

4.3 Discussion of the results

Experimental verification was done to check the correct delivery of the beam since many problems occurred in past years when spot energy was too low due to the overlapping region of patches. Due to limited time available at the gantry, since for experimental verification can be done only during night. We have been forced to take the decision to simulate only two plans, 17914 and 16254.

In order to deliver properly a patch field, it was not possible to follow the normal procedure; in fact the main problem was to leave the couch move while keeping the experimental mode on. We solved this problem generating new steering files with a starting couch position fixed and set on the first experimental session. New patch isocenter positions were calculated and inserted for all fields of all plans.

Two-dimensional gamma analysis (with the criteria of 3%/3mm [58]) were performed between the measurements and the retrospectively calculated dose distribution, of the 3D plan, to quantify the quality of agreement between the 4D delivery and static plan.

The plan of the patient 17914 had 2 fields really similar to each other, as it is possible to see in figure 4.4, but they gave different results, as it is shown in Tables 4.1 and 4.3. No good explanation was found to justify this different behavior. A similarity was found in time to delivery both fields as it is possible to see in Tables 4.2 and 4.4.

The plan of the patient 16254 was a more interesting as case as it has a field that needs 4 patches so region that can achieve a maximum of 32 rescans. For this motivation Field 2 was delivered in all possible combinations and with strong motion simulation, Field 1 was only tested in few combinations to verify the correct delivery. Very good results were obtained for F2 in all setup combinations as it is possible to see in Table 4.5, especially with mitigation of motion involved. Strong motion still gave good results and indications regarding a benefit induced by the increase of overlapping regions have emerged, confirming the analytical results. Time to delivery F2 were comparable with 17914 one (Table 4.6. By Figure 4.5 it emerges that, even in the most critical situations,

there is no degradation of the dose around the patching zone, also in the region of $4cm^2$ that receives 32 rescans.

Also with the benefit induced with 8 rescans and patching, it doesn't seem practical due to large irradiation times, it is suggested to use this combination only if really needed, otherwise 4 rescans should be used.

Conclusions

In this thesis, we investigated the feasibility to deliver 4D treatment plans when it is required the use of patches. The verifications were done in analytical and experimental way.

For the analytical part, it was first necessary to create a tool that allows the visualization of the patch area, to permit a first rough verification, visualizing the dose calculation. There were no inhomogeneities of visible dose. A new procedure for 4DDC was realized during this work to allow to have different setups, as in a normal procedure it is possible to change only the number of rescans. By the results obtained it is possible to say that for small respiratory motion (under 2 mm), no mitigation of the motion is needed, for moderate motion (between 2 and 10 mm), some mitigation of the motion is needed, but also that 4 rescans are enough. Size of the patch overlap does not appear to influence the outcome in a systematic fashion, however, there were some cases, especially for strong motion, where 2cm overlap showed better results.

Experimental delivery required particular attention to the generation of the steering files since it was not possible to proceed with standard procedure, as the couch had to move. Measured data doesn't show any remarkable dose degradation within the overlap area and good gamma scores were achieved. The only problem that emerged was a strange behavior with F2 of patient 17914 that performed bad, while the really similar F1 of the same patient achieved good results. It was not possible to understand the motivations behind those differences. The only field delivered with strong motion

simulation gave results that indicated the benefit of using larger overlap. Combination of 8 rescans and patching doesn't seem practical due to large irradiation times.

An outlook for this study will be certain to add more patient's data when available to give more robustness to the study. Another improvement that will be done in next period is to produce 4DDC log files based, so that the experimental verification will be 3D and not only 2D, as it is with normal gamma analysis obtained by a revelator.

In order to improve the 4D workflow we have designed a new version of the MATLAB script to select the correct mid-ventilation phase. Now it is possible to make more sophisticated analysis, taking into account the presence of metastasis and that those can move in a different way respect to each other.

After this work, it is possible to proceed with the introduction in the clinic procedure the treatment of 4D patients that require patches.

Acronyms

4DDC	4D Dose Calculation
CBCT	Cone Beam Computed Tomography
CGE	Cobalt Grey Equivalent
CPT	Center for Proton Therapy
CT	Computed Tomography
CTV	Clinical Target Volume
DD	Dose Difference
DTA	Distance-To-Agreement
DVH	Dose-Volume Histogram
GTV	Gross Tumor Volume
IMPT	Intensity Modulated Proton Therapy
IR	InfraRed
ITV	Internal Target Volume
LET	Linear Energy Transfer
MFO	Multi-Field Optimization
MP	Motion Phase
OAR	Organ At Risk
PBS	Pencil Beam Scanning
PET	Positron Emission Tomography
PSI	Paul Scherrer Institute
PTV	Planning Target Volume
RBE	Relative Biological Effectivness
RPSP	Relative Proton Stopping Power
SFGen	Steering Files Generator
SFUD	Single Field Uniform Dose
SOBP	Spread-Out Bragg Peak
TPS	Treatment Planning System
TS	Time Stamp

Bibliography

[1] "Radiological Use of Fast Protons", R. R. Wilson, Radiology, 47:487-491 (1946)

[2] Cristofolini M (2015) "La proton terapia una nuova opportunità di cura e ricerca" - LILT

[3] Paganetti H (2011) "Proton Therapy Physics." - CRC Press

[4] Janni JF (1982) "Proton Range-Energy Tables, 1 keV-10 GeV, Energy Loss, Range, Path Length, Time-of-Flight, Straggling, Multiple Scattering, and Nuclear Interaction Probability. Part I. For 63 Compounds." - Atomic Data and Nuclear Data Tables; 27:147, doi:10.1016/0092-640X(82)90004-3

[5] Schneider U, Pedroni E and Lomax AJ (1996) "The calibration of CT Houns

eld units for radiotherapy treatment planning." - Physics in Medicine and Biology; 41(1):111, doi:10.1088/0031-9155/41/1/009

[6] Yang M, Zhu XR, Park PC, Titt U, Mohan R, Virshup G, Clayton GE and Dong L (2012) "Comprehensive analysis of proton range uncertainties related to patient stopping-power-ratio estimation using the stoichiometric calibration." - Phys Med Biol; 57(13):4095-115, doi:10.1088/0031- 9155/57/13/4095

[7] ICRU (1979) "Quantitative Concepts and Dosimetry in Radiobiology (Report 30)." - Journal of the ICRU

[8] Goodhead DT "Radiation eects in living cells." - Canadian Journal of Physics; 68(9):872-886, doi:10.1139/p90-125

[9] ICRU (2007) "Prescribing, Recording, and Reporting Proton-Beam Therapy (ICRU Report 78)." - Journal of the ICRU

[10] Tepper J, Verhey L, Goitein M and Suit HD (1977) "In vivo determinations of RBE in a high energy modulated proton beam using normal tissue reactions and fractionated dose schedules." - Int J Radiat Oncol Biol Phys; 2(11-12):1115-22, doi:10.1016/0360-3016(77)90118-3

[11] U. Amaldi. Particle accelerators: from Big Bang Physics to Hadron Therapy. Springer, 2015.

[12] Pedroni E, Bearpark R, Bohringer T, Coray A, Duppich J, Forss S, George D, Grossmann M, Goitein G, Hilbes C, Jermann M, Lin S, Lomax AJ, Negrazus M, Schippers M and Kotrle G (2004) "The PSI Gantry 2: a second generation proton scanning gantry." - Zeitschrift fur Medizinische Physik, doi:10.1078/0939-3889-00194

[13] Schaatti A, Meer D and Lomax AJ (2014) "First experimental results of motion mitigation by continuous line scanning of protons." - Phys Med Biol; 59(19):5707-23, doi:10.1088/0031-9155/59/19/5707

[14] Scandurra D, Albertini F, van der Meer R, Meier G, Weber DC, Bolsi A and Lomax AJ (2016) "Assessing the quality of proton PBS treatment delivery using machine log

les: comprehensive analysis of clinical treatments delivered at PSI Gantry 2." - Phys Med Biol; 61(3):1171-81, doi:10.1088/0031-9155/61/3/1171

[15] Varian Medical Systems: http://www.varian.com

[16] A. Koschik, C. Baumgarten, C. Bula, J.P. Duppich, A. Gerbershagen, M. Grossmann, *et al.*, "PSI Gantry 3: Integration of a New Gantry into an Existing Proton Therapy Facility",in *Proc. 7th Int. Particle Accelerator Conf. (IPAC'16)*, Busan, Korea, May 2016, paper TUPOY014, pp. 1927–1929, doi:10.18429/JACoW-IPAC2016-TUPOY014, 2016.

[17] "The SC cyclotron and beam lines of PSI's new protontherapy facility PROSCAN" J.M.Schippers R.Dölling J.Duppich G.Goitein M.Jermann A.Mezger E.Pedroni H.W.Reist V.Vrankovic https://doi.org/10.1016/j.nimb.2007.04.052

[18] Schippers, Jacobus and Vranković, Vjeran and George, David (2003), S145-S147, "Beam-dynamics studies in a 250 MeV superconducting cyclotron with a particle tracking program", Nukleonika (48).

[19] Koehler AM, Schneider RJ and Sisterson JM (1975) "Range modulators for protons and heavy ions." - Nuclear Instruments and Methods; 131(3):437-440, doi:10.1016/0029-554X(75)90430-9

[20] Pedroni E, Bacher R, Blattmann H, Bohringer T, Coray A, Lomax AJ, Lin S, Munkel G, Scheib S, Schneider U and Tourovsky A (1995) "The 200-MeV proton therapy project at the Paul Scherrer Institute: Conceptual design and practical realization." - Med Phys; 22:37, doi:10.1118/1.597522

[21] Kanai T, Kawachi K, Kumamoto Y, Ogawa H, Yamada T, Matsuzawa H and Inada T (1980) "Spot scanning system for proton radiotherapy." - Med Phys; 7(4):365-9, doi:10.1118/1.594693

[22] Lomax AJ, Bohringer T, Bolsi A, Coray D, Emert F, Goitein G, Jermann M, Lin S, Pedroni E, Rutz H, Stadelmann O, Timmermann B, Verwey J and Weber DC (2004) "Treatment planning and veri

cation of proton therapy using spot scanning: initial experiences." - Medical Physics; 31(11):3150-7, doi:10.1118/1.1779371

[23] Lomax AJ (1999) "Intensity modulation methods for proton radiotherapy." - Physics in Medicine and Biology; 44(1):185-205

[24] Lomax AJ (2008) "Intensity modulated proton therapy and its sensitivity to treatment uncertainties 2. The potential effects of inter-fraction and inter

led motion." - Phys Med Biol; 53(4):1043-56, doi:10.1088/0031-9155/53/4/015

[25] Albertini F, Gaignat S, Bosshardt M and Lomax AJ (2009) "Planning and Optimizing Treatment Plans for Actively Scanned Proton Therapy." - Biomedical Mathematics Promising Directions in Imaging, Therapy Planning, and Inverse Problems ed Y Censor, M Jiang and G Wang (Madison,WI: Medical Physics Publishing) pp 1-18

[26] https://www.psi.ch/protontherapy/center-for-proton-therapy-cpt

[27] Sairos Safai and Christian Bula and David Meer and Eros Pedroni, "Improving the precision and performance of proton pencil beam scanning", Translational Cancer Research, http://tcr.amegroups.com/article/view/599

[28] Leroy, Roos and Benahmed, Nadia and Hulstaert, Frank and Mambourg, Françoise and Fairon, Nicolas and Van Eycken, Elisabeth and De Ruysscher, Dirk, "Hadron therapy in children – an update of the scientific evidence for 15 paediatric cancers."

[29] Mayo JR, Muller NL, Henkelman RM: The double-fissure sign: A motion artifact on thin-section CT scans. Radiology 165:580-581, 1987

[30] Minohara S, Kanai T, Endo M, et al: Respiratory gatedirradiation system for heavy-ion radiotherapy. Int J Radiat Oncol Biol Phys 47:1097-1103, 2000

[31] Yorke ED, Wang L, Rosenzweig KE, et al: Evaluation of deep inspiration breath-hold lung treatment plans with Monte Carlo dose calculation. Int J Radiat Oncol Biol Phys 53:1058-1070, 2002

[32] Keall P, "4-Dimensional Computed Tomography Imaging and Treatment Planning", Seminars in Radiation Onclogy, 10.1053/j.semradonc.2003.10.006

[33] Vedam SS, Keall PJ, Kini VR, et al: Acquiring a four dimensional computed tomography dataset using an external respiratory signal. Phys Med Biol 48:45-62, 2003

[34] Hill DL, Batchelor PG, Holden M, et al: Medical image registration. Phys Med Biol 46:R1-45, 2001

[35] 4ICRU, "Prescribing, recording and reporting photon beam therapy (supplement to ICRU Report 50)," ICRU Report No. 62 (International Commission on Radiation Units and Measurements, Bethesda, MD, 1999.

[36] D. L. Mc Shan, M. L. Kessler, K. Vineberg, and B. A. Fraass, "Inverse plan optimization accounting for random geometric uncertainties with a multiple instance geometry approximation (MIGA)," Med. Phys. 32(5), 1510–1521 (2005).

[37] P. J. Keall, G. S. Mageras, J. M. Balter, R. S. Emery, K. M. Forster, S. B. Jiang, J. M. Kapatoes, D. A. Low, M. J. Murphy, B. R. Murray, C. R. Ramsey, M. B. Van Herk, S. S. Vedam, J. W. Wong, and E. Yorke, "The management of respiratory motion in radiation oncology report of AAPM Task Group 76," Med. Phys. 33(10), 3874–3900 (2006).

[38] M. Phillips, E. Pedroni, H. Blattmann, T. Boehringer, A. Coray, and S. Scheib, "Effects of respiratory motion on dose uniformity with a charged particle scanning method," Phys. Med. Biol. 37(1), 223–234 (1992).

[39] J. Seco, D. Robertson, A. Trofimav, and H. Paganetti, “Breathing interplay effects during proton beam scanning: Simulation and statistical analysis,” Phys. Med. Biol. 54, N283–N294 (2009).

[40] H. D. Kubo and B. C. Hill, “Respiration gated radiotherapy treatment: A technical study,” Phys. Med. Biol. 41, 83–91 (1996).

[41] M. Murphy, “Tracking moving organs in real time,” Semin. Radiat. Oncol. 14(1), 91–100 (2004).

[42] C. A. Kelsey, ”Radiation biology in medical imaging” - Wiley Blackwell (2014)

[43] Kavanagh, Joy and Redmond, Kelly and Schettino, Giuseppe and Prise, Kevin, ”DSB Repair - A radiation perspective.”, Antioxidants redox signaling, 2013-01, doi: 10.1089/ars.2012.5151

[44] Yuh G E, Loredo L N, Yonemoto L T, Bush D A, Shahnazi K, Preston W, Slater J M and Slater J D 2004 ”Reducing toxicity from craniospinal irradiation: using proton beams to treat medulloblastoma in young children Cancer” J. 10 386–90

[45] Hug E B, Nevinny-Stickel M, Fuss M, Miller D W, Schaefer R A and Slater J D 2001 ”Conformal proton radiation treatment for retroperitoneal neuroblastoma: introduction of a novel technique” Med. Pediatr. Oncol. 37 36–41

[46] Inaniwa T, Kanematsu N, Furukawa T and Noda K 2011 ”Optimization algorithm for overlapping-field plans of scanned ion beam therapy with reduced sensitivity to range and setup uncertainties” Phys. Med. Biol. 56 1653

[47] Titt U, Mirkovic D, Sawakuchi G O, Perles L A, Newhauser W D, Taddei P J and Mohan R 2010 ”Adjustment of the lateral and longitudinal size of scanned proton beam spots using a pre-absorber to optimize penumbrae and delivery efficiency” Phys. Med. Biol. 55 7097

[48] Bula C, Meer D and Pedroni E 2013 "A system for the delivery of proton therapy by pencil beam scanning of a predeterminable volume within a patient" WO Patent App. PCT/EP2013/056,732

[49] G Meier and R Besson and A Nanz and S Safai and A J Lomax "Independent dose calculations for commissioning, quality assurance and dose reconstruction of PBS proton therapy", Physics in Medicine and Biology 60-7, doi: 10.1088/0031-9155/60/7/2819

[50] Gomà C, Lorentini S, Meer D and Safai S 2014 Proton beam monitor chamber calibration Phys. Med. Biol. 59 4961–71

[51] S. Van de Water, R. Kreuge, S. M. Zenklusen, E. Hug, and A. J. Lomax, "Tumour tracking with scanned proton beams: Assessing the accuracy and practicalities," Phys. Med. Biol. 54, 6549–6563 (2009).

[52] B. Schaffner, E. Pedroni, and A. Lomax, "Dose calculation models for proton treatment planning using a dynamic beam delivery system: An attempt to include density heterogeneity effects in the analytical dose calculation," Phys. Med. Biol. 44, 27–41 (1999).

[53] D. Boye, A. J. Lomax, A. Knopf, "Mapping motion from 4D-MRI to 3D-CT for use in 4D dose calculations: A technical feasibility study", Med. Phys. 40(6) 2013, DOI: 10.1118/1.4801914.

[54] R. Zhang, P. J. Taddei, M. M. Fitzek, and W. D. Newhauser, "Water equivalent thickness values of materials used in beams of protons, helium, carbon and iron ions", Phys Med Biol. 2010 May 7; 55(9). doi:10.1088/0031-9155/55/9/004.

[55] https://www.ptw.de

[56] https://www.ndigital.com/medical/products/polaris-family/

[57] G. Fattori, S. Safai, P. Fernández Carmona, M. Peroni, R. Perrin, D. C. Weber and A. J. Lomax, "Monitoring of breathing motion in image-guided PBS proton therapy: comparative analysis of optical and electromagnetic technologies", Radiation Oncology (2017) 12:63, DOI 10.1186/s13014-017-0797-9

[58] Ezzell GA, Burmeister JW, Dogan N, LoSasso TJ, Mechalakos JG, Mihailidis D, Molineu A, Palta JR, Ramsey CR, Salter BJ, Shi J, Xia P, Yue NJ, Xiao Y, "IMRT commissioning: multiple institution planning and dosimetry comparisons, a report from AAPM Task Group 119" Med Phys. 2009 Nov; 36(11):5359-73

[59] Daniel A. Low, William B. Harms, Sasa Mutic, and James A. Purdy, "A technique for the quantitative evaluation of dose distributions", Med. Phys., 25 (1998) 656, doi: 10.1118/1.598248